

LatentTrack: Sequential Weight Generation via Latent Filtering

Omer Haq¹

Abstract

We introduce *LatentTrack* (LT), a sequential neural architecture for online probabilistic prediction under nonstationary dynamics. LT performs causal Bayesian filtering in a low-dimensional latent space and uses a lightweight hypernetwork to generate predictive model parameters at each time step, enabling constant-time online adaptation without per-step gradient updates.

At each time step, a learned latent model predicts the next latent distribution, which is updated via amortized inference using new observations, yielding a predict–generate–update filtering framework in function space. The formulation supports both structured (Markovian) and unstructured latent dynamics within a unified objective, while Monte Carlo inference over latent trajectories produces calibrated predictive mixtures with fixed per-step cost. Evaluated on long-horizon online regression using the Jena Climate benchmark, LT consistently achieves lower negative log-likelihood and mean squared error than stateful sequential and static uncertainty-aware baselines, with competitive calibration, demonstrating that latent-conditioned function evolution is an effective alternative to traditional latent-state modeling under distribution shift.

1. Introduction

LT in a nutshell. LT is a *filter in function space*: instead of filtering over observations or outputs, it tracks a low-dimensional latent state z_t whose dynamics generate the evolving weights of a predictive model. A learned transition predicts z_t , a hypernetwork maps z_t to model parameters θ_t , and new data update an amortized posterior over z_t . This predict–generate–update cycle performs online inference directly over *functions*, enabling continual adaptation and

^{*}Equal contribution ¹Independent Researcher, Baltimore, MD, USA. Correspondence to: Omer Haq <haqomer1@gmail.com>.

Proceedings of the 43rd International Conference on Machine Learning, Seoul, South Korea. PMLR 306, 2026. Copyright 2026 by the author(s).

calibrated uncertainty without retraining. Predictive uncertainty arises naturally from Monte Carlo mixtures over latent trajectories, yielding temporally coherent predictions with constant-time test-time updates.

Scope. We focus on supervised streaming settings with known covariates, i.e., $\mathcal{D}_t = (x_t, y_t)$ observed at predict time. The framework applies broadly to regression, classification, and value or policy heads, though we do not model covariate dynamics.

Filtering and beyond. While our empirical evaluation focuses on causal online filtering, the LT framework naturally extends to forecasting and open-loop generation by rolling forward the learned latent transition. We focus on filtering to isolate stability and adaptation under distribution shift, but LT is best viewed as a general latent dynamical model over predictive functions.

Capacity allocation and structural learning. A central design choice in LT is how representational capacity is allocated. Rather than increasing the expressivity of latent inference components such as the prior, posterior, or transition, LT concentrates capacity in a hypernetwork that maps latent states to predictive functions. This shifts modeling burden from latent inference to function generation, allowing relatively simple latent dynamics to control a rich and flexible hypothesis class. We hypothesize that this allocation yields more stable adaptation, improved pointwise accuracy, stronger predictive likelihood, and better-calibrated uncertainty under nonstationarity than architectures that rely on increasingly expressive latent dynamics.

Contributions and novelty.

- **Function-space filtering.** A framework for sequential Bayesian filtering in latent weight space, tracking an evolving generator of predictive functions.
- **Predict–generate–update objective.** A filtering ELBO derived from streaming evidence, supporting both structured (Markovian) and unstructured latent dynamics.
- **Structural learning via weight generation.** A capacity allocation that concentrates expressivity in function generation rather than latent inference, enabling stable online adaptation with calibrated uncertainty.

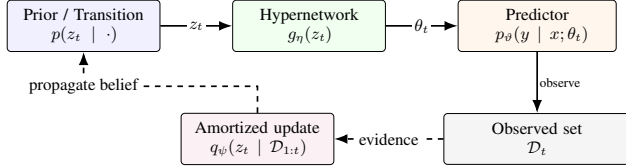


Figure 1. LT predict–generate–update loop (supervised setting). A latent belief z_t is propagated via a causal prior/transition conditioned on a running summary of past observations, mapped to predictor parameters θ_t by the hypernetwork g_η , and used to define the predictive model $p_\theta(y_t | x_t; \theta_t)$. Incoming observations then amortize a posterior update over z_t , enabling temporally causal belief filtering over predictor parameters.

- **Constant-time adaptation.** $\mathcal{O}(1)$ per-step inference via amortized updates, with no test-time gradients or inner-loop optimization.
- **Fair evaluation.** A capacity–compute matching protocol that equalizes parameters and predictive samples across methods.
- **Empirical validation.** On long-horizon online regression using real-world climate data, LT achieves lower error on the majority of time steps, improved robustness across random seeds, and well-behaved predictive uncertainty relative to stateful and static baselines.

2. Method

2.1. Setup (General \mathcal{D})

We observe a stream $\mathcal{D}_{1:T} = (\mathcal{D}_1, \dots, \mathcal{D}_T)$, where each \mathcal{D}_t may be a singleton or a mini-batch. LT posits a low-dimensional latent state $z_t \in \mathbb{R}^d$ with emission $p(\mathcal{D}_t | z_t)$. When \mathcal{D}_t contains supervised pairs, a lightweight hypernetwork g_η maps z_t to predictor weights $\theta_t = g_\eta(z_t)$ used in the emission (see Section 2.4). We defer any discussion of controlled/summary states to Section 2.5.

2.2. Prior Predictive and One-Step Prior

By the conditional independence $(\mathcal{D}_t \perp \mathcal{D}_{1:t-1}, z_{1:t-1}) | z_t$, the one-step evidence is

$$p(\mathcal{D}_t | \mathcal{D}_{1:t-1}) = \int p(\mathcal{D}_t | z_t) p_\phi(z_t | \mathcal{D}_{1:t-1}) dz_t. \quad (1)$$

Here $p_\phi(z_t | \mathcal{D}_{1:t-1})$ denotes the *one-step prior*: any causal distribution over z_t that depends only on past data $\mathcal{D}_{1:t-1}$.

2.3. Filtering ELBO (general, \mathcal{D} -only)

Applying Jensen’s inequality to $\log p(\mathcal{D}_t | \mathcal{D}_{1:t-1})$ with the amortized posterior $q_\psi(z_t | \mathcal{D}_{1:t})$ gives the per-step filtering

ELBO

$$\mathcal{L}_t = \mathbb{E}_{q_\psi(z_t | \mathcal{D}_{1:t})} [\log p(\mathcal{D}_t | z_t)] - \text{KL}(q_\psi(z_t | \mathcal{D}_{1:t}) \| p_\phi(z_t | \mathcal{D}_{1:t-1})). \quad (2)$$

Summing over t yields $\sum_{t=1}^T \mathcal{L}_t \leq \log p(\mathcal{D}_{1:T})$ by the chain rule.

Structured replacement. A looser but often more stable variant replaces the marginal prior in the KL with the transition kernel conditioned on the previous latent:

$$\begin{aligned} \text{KL}(q_\psi(z_t | \mathcal{D}_{1:t}) \| p_\phi(z_t | \mathcal{D}_{1:t-1})) &\Rightarrow \\ \mathbb{E}_{q_\psi(z_{t-1} | \mathcal{D}_{1:t-1})} [\text{KL}(q_\psi(z_t | \mathcal{D}_{1:t}) \| p_\phi(z_t | z_{t-1}, \mathcal{D}_{1:t-1}))]. \end{aligned} \quad (3)$$

Here the outer expectation is with respect to $z_{t-1} \sim q_\psi(z_{t-1} | \mathcal{D}_{1:t-1})$. This replacement yields the *structured ELBO*; see Appendix A for the full derivation.

Structured vs. original KL. The structured replacement encourages *temporal coherence* by aligning the posterior at step t to the *transition kernel* from z_{t-1} , empirically reducing latent drift and stabilizing training. It also regularizes the transition parameters ϕ more directly (the prior is judged on its one-step predictions), often producing smoother z_t trajectories. The trade-off is that the bound is *looser* (by KL convexity), so it can understate misfit to the marginalized prior, and optimization inherits extra variance from the outer expectation over z_{t-1} (or its samples). Practically, it adds mild compute (sampling/integrating over z_{t-1}) and can be more sensitive when the transition is misspecified; in such cases the original marginal-KL objective may provide a crisper likelihood signal.

We denote the transition-conditioned objective in Equation (3) as *LT-Structured* (LT-Structured), emphasizing explicit temporal structure in the latent dynamics, and the original marginal-prior formulation as *LT-Unstructured* (LT-Unstructured).

2.4. Specializing $\mathcal{D}_t = (x_t, y_t)$

For supervised pairs $\mathcal{D}_t = (x_t, y_t)$, the emission factorizes as

$$p(\mathcal{D}_t | z_t) = p(y_t, x_t | z_t) = p(y_t | x_t, z_t) p(x_t | z_t), \quad (4)$$

with $p(y_t | x_t, z_t)$ parameterized by $\theta_t = g_\eta(z_t)$ (e.g., Gaussian mean $f_{\theta_t}(x_t)$ and noise head $\Sigma_{\theta_t}(x_t)$ for regression, categorical/Bernoulli heads for classification, or value/advantage heads for RL targets).

Known-covariate assumption (one-step forecasting). If x_t is observed at predict time and we do not model its

process, $p(x_t | \mathcal{D}_{1:t-1}) = \delta_{x_t^*}(x_t)$ and

$$p(\mathcal{D}_t | \mathcal{D}_{1:t-1}) = p(y_t | x_t, \mathcal{D}_{1:t-1}), \quad (5)$$

$$p(y_t | x_t, \mathcal{D}_{1:t-1}) = \int p_\theta(y_t | x_t; g_\eta(z_t)) p_\phi(z_t | \mathcal{D}_{1:t-1}) dz_t. \quad (6)$$

Under this assumption, (2) specializes to

$$\begin{aligned} \mathcal{L}_t = & \mathbb{E}_{q_\psi(z_t | \mathcal{D}_{1:t})} [\log p_\theta(y_t | x_t; g_\eta(z_t))] \\ & - \text{KL}\left(q_\psi(z_t | \mathcal{D}_{1:t}) \parallel p_\phi(z_t | \mathcal{D}_{1:t-1})\right). \end{aligned} \quad (7)$$

Equation (7) therefore defines the core training step of LT: an online evidence lower bound that performs amortized Bayesian filtering over latent-generated weights. This objective underlies the *predict–generate–update* loop, illustrated schematically in Figure 1 for the online regression and filtering setting, where the latent prior/transition distribution is conditioned causally on the running summary of past observations.

2.5. Online training & inference: variants and credit weighting

Causal sequence backbone. LT assumes a causal summarizer that maintains a fixed-size state $h_t = h_\psi(h_{t-1}, e_t)$ from encoded observations $e_t = \text{Enc}_\psi(\mathcal{D}_t)$. Any backbone exposing this interface is compatible with the framework. All experiments in this work use a gated recurrent unit (GRU), which provides stable updates under nonstationarity with constant per-step memory. This choice is orthogonal to LT’s probabilistic components: the prior and posterior heads consume the summarizer state without imposing assumptions on its internal structure.

Online training and inference. LT operates in an online setting, using variational filtering during training and streaming prediction at inference. In all experiments, training is performed with chunked truncated backpropagation through time (TBPTT) over a fixed window (Algorithm 2), which bounds gradient horizon while maintaining low latency. Within each window, per-step ELBOs are combined using fixed recency weighting to prioritize recent observations. Alternative training schedules and weighting schemes are described in Appendix B.

At test time, the unstructured variant predictions are generated using the prior path only. Given the causal summary h_{t-1} , the prior head $\text{Head}_{p_\phi}(h_{t-1})$ outputs parameters $(\mu_t^{(p)}, \log \sigma_t^{(p)})$ defining $p_\phi(z_t | h_{t-1})$. We draw K samples $z_t^{(k)} \sim \mathcal{N}(\mu_t^{(p)}, \text{diag}(\sigma_t^{(p)2}))$, map them through the hypernetwork to $\theta_t^{(k)} = g_\eta(z_t^{(k)})$, and form the predictive mixture

$$\hat{p}(y_t | x_t, \mathcal{D}_{1:t-1}) \approx \frac{1}{K} \sum_{k=1}^K p_\theta(y_t | x_t; \theta_t^{(k)}).$$

For Gaussian heads, this yields predictive mean $\hat{\mu}_t(x_t) = \frac{1}{K} \sum_k \mu_{\theta_t^{(k)}}(x_t)$ and variance $\hat{\sigma}_t^2(x_t) = \frac{1}{K} \sum_k \sigma_{\theta_t^{(k)}}^2(x_t) + \text{Var}_k[\mu_{\theta_t^{(k)}}(x_t)]$, corresponding to aleatoric and epistemic components. After observing \mathcal{D}_t , the summary state is updated causally without gradients, $h_t = h_\psi(h_{t-1}, \text{Enc}_\psi(\mathcal{D}_t))$, so subsequent predictions incorporate the new information.

3. Complexity, Capacity, and Fairness

To ensure fair and interpretable comparisons, we control model capacity, training protocol, and inference-time cost across baselines while respecting structural differences between stateful and static models. Detailed hyperparameters and parameter count are provided in Appendix D, Table 2, 3.

Training protocol. All models are trained for 6 epochs and evaluated over 25 random seeds. Extending training to 20 epochs on a subset of seeds yields no material improvement, with performance saturating after approximately 4 epochs. The 6-epoch budget therefore exceeds convergence while limiting overfitting and computational variance.

Stateful models (LT, VRNN, DSSM) are trained using TBPTT with window length $W=256$ and fixed recency weighting $\lambda=0.9$. Latent and hidden dimensions are held constant across stateful methods ($\dim(z_t)=8$, $\dim(h_t)=64$) to isolate architectural differences rather than state size.

Static baselines (MC-Dropout, Bayes-by-Backprop, Deep Ensembles) are trained on overlapping sliding windows of length $W=256$ with stride $S=32$ and the same recency weighting. This results in approximately $8\times$ more parameter updates per epoch and greater context overlap, which can improve optimization stability but does not preserve persistent temporal state.

KL scheduling. All stochastic models use linear β -annealing with $\beta_{\text{max}}=1$. Warmup horizons are aligned in terms of effective training progress: $\beta_{\text{warmup}}=575$ updates for stateful models and $\beta_{\text{warmup}}=4600$ for static models (approximately 3 epochs), ensuring comparable regularization strength across update cadences.

Capacity allocation and inference-time matching. LT generates the *entire* predictor network at each time step via a hypernetwork conditioned on z_t , requiring deliberate capacity reallocation. Compared to VRNN and DSSM, LT employs lightweight linear-Gaussian prior, posterior, and transition heads, allocating most parameters to predictive weight generation. This reflects the core hypothesis of LT—that modeling nonstationarity through function evolution is more effective than increasing latent inference expressivity—while remaining matched in total capacity and test-time cost.

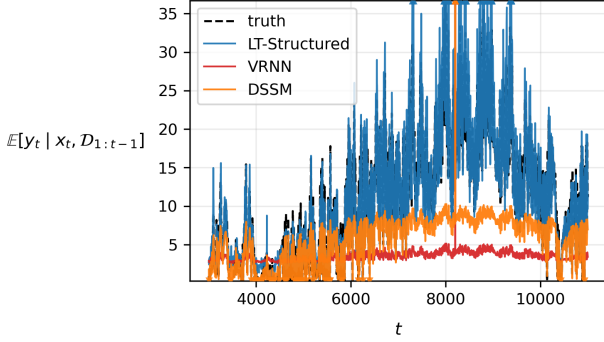


Figure 2. Predictive mean over time for the representative seed. LT tracks the signal more accurately than stateful baselines, but exhibits occasional instability consistent with the failure-rate statistics.

All methods are matched by inference-time parameter count and predictive sampling budget. Total parameters are constrained to approximately 20k ($\pm 10\%$), with stricter matching of *active test-time parameters* to 20k ($\pm 5\%$), excluding components not used during inference (e.g., amortized posteriors in DSSM and LT-Unstructured). Predictive sampling is equalized, with non-ensemble methods using $K=1$ sample during training and $K=100$ at evaluation. Deep Ensembles using $M=10$ members throughout.

4. Experiments

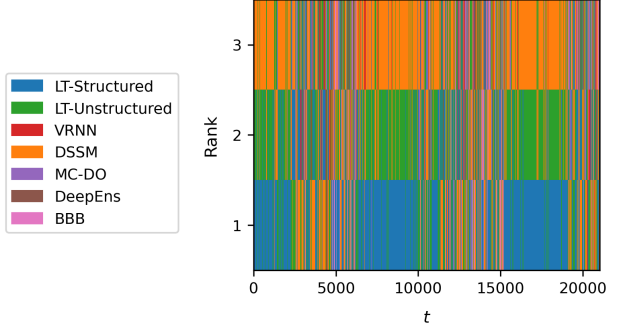
4.1. Task and Stream

We evaluate LT on long-horizon online prediction using the **Jena Climate** dataset, a real-world multivariate time series with strong seasonality and nonstationary drift. The dataset contains 14 meteorological variables recorded hourly; we downsample by a factor of 6 to obtain 6-hour resolution. At each time step, the model predicts temperature 6 steps ahead (36 hours), conditioned on a rolling history of past observations and known time-of-day and day-of-week covariates.

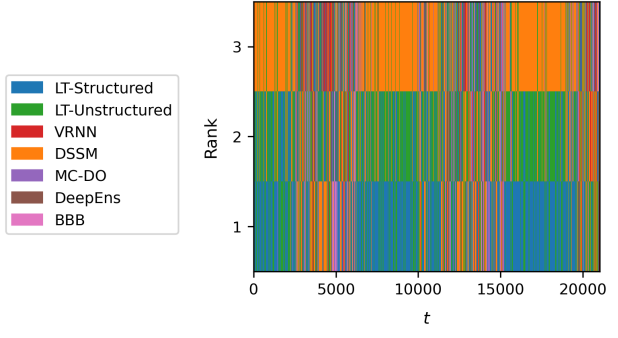
LT operates in strictly causal filtering mode: predictions at time t use data up to $t-1$, after which the latent state is updated upon observing D_t . The first 70% of the sequence is used for training, with evaluation performed on the remaining 30%, which includes substantial seasonal transitions and regime changes. Performance is assessed continuously over the evaluation stream, reflecting realistic online deployment without retraining or test-time optimization.

4.2. Baselines

We compare **LT** against both stateful sequential models and static uncertainty-aware baselines. As sequential baselines, we include Variational Recurrent Neural Networks



(a) Temporal NLL Top 3 Winners Grid



(b) Temporal MSE Top 3 Winner Grid

Figure 3. Ranking stability across time. Colors indicate the top-3 models at each time step. (a) Per-time-step negative log-likelihood (NLL) ranking. (b) Per-time-step mean squared error (MSE) ranking. Lower ranks indicate better performance. LT-Structured appears more frequently among the top-ranked methods across time, indicating greater ranking stability under both metrics.

(VRNNs) (Chung et al., 2015; Fraccaro et al., 2016), which combine recurrent dynamics with per-step latent variables trained via amortized variational inference, and Deep State-Space Models (DSSMs) (Krishnan et al., 2015; Karl et al., 2017; Doerr et al., 2018; Rangapuram et al., 2018b), which couple latent Markov dynamics with neural parameterizations of transitions and emissions. We also evaluate static uncertainty baselines, including MC-Dropout (Gal & Ghahramani, 2016), Deep Ensembles (Lakshminarayanan et al., 2017), and Bayes-by-Backprop (BBB) (Blundell et al., 2015). Full model specifications, parameterizations, and training details for VRNN and DSSM are provided in Appendix C.

4.3. Metrics and Evaluation

We evaluate predictive accuracy, uncertainty quality, and temporal stability using negative log-likelihood (NLL) and mean squared error (MSE) computed over full streaming sequences. For each random seed, we compute temporal

Representative Seed: Temporal Metrics Across Time						
Model	Negative Log-Likelihood (NLL)					
	Mean ↓	Trimmed Mean ↓	Median ↓	Trimmed Median ↓	% Rank-1 ↑	% Rank ≥ 2 ↑
LT (Structured)	6.29	2.44	2.33	2.32	58.8	79.6
LT (Unstructured)	1.22×10^{10}	2.73	2.62	2.61	17.6	65.8
DSSM	2.97	2.87	2.95	2.93	17.8	38.1
VRNN	3.44	3.41	3.39	3.38	0.9	4.6
MC-Dropout	23.19	10.92	4.56	4.49	0.9	3.4
Deep Ensembles	29.85	28.27	10.62	10.14	0.1	1.2
BBB	19.20	17.57	8.24	7.86	3.9	7.4
Mean Squared Error (MSE)						
Model	Mean ↓	Trimmed Mean ↓	Median ↓	Trimmed Median ↓	% Rank-1 ↑	% Rank ≥ 2 ↑
LT (Structured)	10095.7	6.32	1.98	1.93	51.4	75.2
LT (Unstructured)	16978.1	16.26	4.68	4.55	23.2	70.1
DSSM	69.68	45.29	15.38	14.82	14.5	31.5
VRNN	112.17	93.25	46.82	45.60	2.5	6.6
MC-Dropout	14906.4	114.46	65.81	64.18	4.0	7.7
Deep Ensembles	1584.85	139.94	76.92	74.61	2.1	3.8
BBB	3543.0	124.60	69.83	68.13	2.3	5.1

Table 1. Single-seed temporal statistics computed over all time steps for the representative seed. Trimmed statistics remove the top 1% of values. **A single data anomaly dominates the untrimmed mean MSE, whereas trimmed and median statistics reflect typical tracking behavior.** Rank percentages indicate the fraction of time steps in which a method achieves the best (Rank-1) or top-two (Rank ≥ 2) performance, emphasizing sustained per-step accuracy rather than sensitivity to isolated outliers.

summaries over the entire horizon, including mean, median, and trimmed variants (excluding the top 1% of values) for both metrics; trimmed and median statistics are emphasized, as temporal means are highly sensitive to rare extreme events. A representative seed for LT-Structured is selected as the one whose temporal mean NLL is closest to the median across seeds. In addition, we report per-time-step rankings for NLL and MSE. Robustness across random initializations is assessed via a catastrophic failure rate, defined as the fraction of seeds whose maximum NLL exceeds 10^6 , isolating rare but severe divergence events. Additional uncertainty diagnostics, including probability integral transform (PIT) histograms, calibration curves, and epistemic/aleatoric variance decompositions, are reported in the appendix and omitted from the main text for brevity, as they are consistent with trends observed in NLL and MSE.

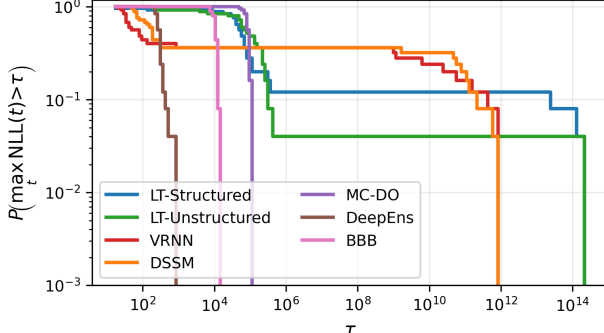
4.4. Results

We evaluate LT under long-horizon online prediction on the Jena Climate benchmark, focusing on four aspects critical for streaming deployment: (i) sustained per-step predictive performance and accuracy rather than aggregate averages, (ii) robustness to catastrophic failures across random initializations, (iii) the role of structured versus unstructured latent dynamics, and (iv) the quality of predictive uncertainty.

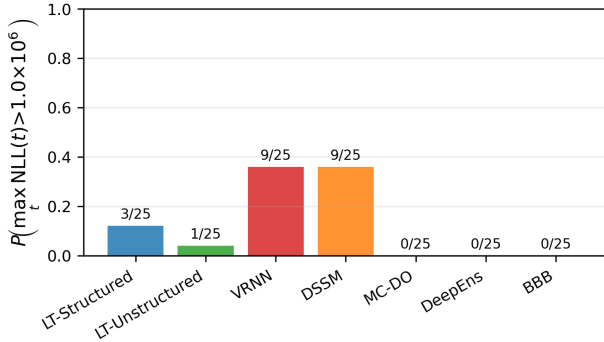
Isolated data anomaly and evaluation implications. During evaluation on the Jena Climate benchmark, we observe a single isolated time step at which all models—including both stateful and static baselines—exhibit extreme predictive error. As shown in Appendix D, (Figures 15, 16, 17, and 18), this event induces a simultaneous spike in prediction error (MSE), negative log-likelihood (NLL), and predictive uncertainty, affecting aleatoric, epistemic, and total variance. The synchronization of this response across all models indicates sensitivity to a shared extreme observation or data anomaly rather than model-specific instability.

Importantly, all models recover immediately following this event, with predictive means and uncertainty returning to baseline levels within a single time step. While such isolated extremes strongly influence temporal means and maximum-based statistics (e.g., CCDF tails), they do not reflect typical per-step behavior over long horizons and therefore should not dominate conclusions about sustained performance. For this reason, we emphasize trimmed and median statistics, together with per-time-step analyses, which more accurately characterize sustained predictive performance and calibration under nonstationary dynamics.

Claim 1: Sustained per-step performance (not averages). Figure 2 shows predictive mean trajectories over a selected interval for the representative seed and the top two baselines.



(a) CCDF of peak per-time-step NLL



(b) Catastrophic failure rate at fixed threshold

Figure 4. Temporal stability and catastrophic failure under distribution shift. (a) Complementary cumulative distribution function (CCDF) of the maximum per-time-step negative log-likelihood, $\max_t \text{NLL}(t)$, computed per run and aggregated across seeds, characterizing the tail behavior of rare but severe prediction failures. (b) Fraction of runs whose peak NLL exceeds a fixed threshold $\tau = 10^6$, corresponding to a vertical slice of the CCDF in (a). LT variants exhibit lighter tails and lower failure rates than stateful baselines, indicating improved robustness to transient instability while maintaining competitive predictive accuracy.

LT-Structured tracks the underlying signal more closely than stateful baselines, particularly during seasonal transitions and regime shifts. Over the full evaluation horizon (Appendix D, Figure 5), LT maintains accurate tracking across extended nonstationary segments.

Table 1 reports temporal statistics for the representative seed, including negative log-likelihood (NLL) and mean squared error (MSE), summarized using means, medians, and trimmed variants that exclude the top 1% of extreme values. Across both metrics, **LT-Structured achieves the strongest median and trimmed performance**, indicating superior typical per-step accuracy and probabilistic quality. These statistics emphasize representative behavior within a single long-horizon deployment, which is more informative than the temporal mean, which in this setting is dominated

by a single isolated data anomaly.

Per-time-step rankings further reinforce this conclusion. As summarized in Table 1 and visualized in Figure 3, LT-Structured achieves first-place ranking for NLL in 58.8% of time steps and ranks second or better in 79.6% of time steps. For MSE, it attains first place in 51.4% of time steps and ranks second or better in 75.2% of time steps. LT-Unstructured also performs favorably, consistently trailing only the structured variant. Together, these results indicate that LT's advantage reflects sustained per-step performance rather than sensitivity to aggregate averaging.

Claim 2: Robustness to nonstationarity across random initializations. To assess robustness across random initializations, we analyze catastrophic failures aggregated over seeds. Figure 4 reports the complementary cumulative distribution function (CCDF) of the maximum per-time-step NLL attained within each run, together with a fixed-threshold failure rate defined as the fraction of seeds whose peak NLL exceeds 10^6 . This analysis isolates rare but severe divergence events that are not reflected in within-run median or ranking statistics and typically associated with the data anomalies discussed above.

Under this criterion, both LT variants exhibit **significantly lower failure probabilities** than VRNN and DSSM, corresponding to fewer runs that experience catastrophic divergence. LT-Unstructured achieves the lowest catastrophic failure probability (4%), followed by LT-Structured (12%), substantially outperforming other stateful models.

While the CCDF indicates that, conditional on failure, LT can exhibit larger peak NLL values than some baselines, we emphasize that such peaks typically occur at the same isolated time steps across all models (Appendix D, Figure 17 and 18). Once the catastrophic threshold is exceeded, the run is already dominated by failure, and differences in peak magnitude (e.g., 10^6 versus 10^{10}) are of limited practical relevance. Accordingly, our robustness analysis focuses on the *frequency* of catastrophic failures across seeds rather than the precise severity of individual divergence events.

Importantly, these failures are transient: NLL, MSE, and predictive variance typically spike for a single time step before rapidly recovering. This behavior indicates sensitivity to abrupt, shared stress points in the sequence rather than persistent model instability. Static baselines also exhibit catastrophic failures under this definition; however, these events are typically less severe in magnitude.

Claim 3: Structured vs. unstructured latent dynamics. Comparing LT variants reveals a stability–accuracy tradeoff rather than a single dominant configuration. LT-Structured achieves slightly stronger median and trimmed NLL and MSE, reflecting improved typical accuracy and temporal

coherence over the majority of time steps. In contrast, LT-Unstructured exhibits the lowest catastrophic failure probability across random initializations (4%), followed by LT-Structured (12%), indicating reduced tail risk under rare misalignment events.

This behavior reflects the role of latent transition structure in shaping error profiles. Enforcing temporal structure improves coherence of the latent trajectory and yields more accurate predictions for most time steps, but can increase sensitivity to rare transition misalignment conditional on failure, when the learned dynamics momentarily fail to track abrupt changes. The unstructured variant, which relies on a marginal prior rather than an explicit transition model, reduces the likelihood of persistent divergence at the cost of slightly weaker typical accuracy.

Importantly, both variants substantially outperform baselines across all evaluation criteria, indicating that the primary gains arise from latent-conditioned weight generation itself rather than the specific form of the latent dynamics.

This tradeoff also manifests in how uncertainty is expressed under extreme observations, with structured and unstructured LT variants allocating uncertainty differently between epistemic and aleatoric components (Claim 4); additional comparisons between the two variants are provided in Appendix D (Figures 9–12).

Claim 4: Well-behaved uncertainty, not overconfidence. The performance gains achieved by LT are not driven by overconfident or miscalibrated uncertainty estimates. Improvements in median and trimmed NLL coincide with stable variance behavior, indicating that predictive accuracy gains arise from better modeling of the data rather than artificial variance inflation.

Additional diagnostics reported in Appendix D support this conclusion. Probability integral transform (PIT) histograms (Figure 14) and calibration curves (Figure 13) show reduced boundary mass and closer adherence to the uniform reference relative to baselines, consistent with improved probabilistic calibration. The calibration curves are computed over the central [1, 99)% predictive mass, ensuring that they reflect typical behavior rather than being dominated by the isolated data anomaly.

Decompositions of predictive uncertainty into aleatoric and epistemic components over time (Figure 6) show that LT maintains stable uncertainty levels over long horizons, with only transient deviations under extreme observations. All stateful models exhibit a synchronized spike in uncertainty at the isolated data anomaly, followed by immediate recovery to baseline levels, indicating short-lived stress rather than persistent miscalibration.

Decompositions of predictive uncertainty into aleatoric and

epistemic components over time (Appendix D, Figure 6) show that LT maintains stable uncertainty levels over long horizons, with transient stress responses concentrated at a single extreme observation. Although all models exhibit a brief peak in total variance, MSE, and NLL at this anomaly (Figures 17–18), the *composition* of that peak differs (Figure 16): LT-Unstructured drives the response almost entirely through an epistemic spike while its aleatoric variance collapses to near-zero, whereas LT-Structured shows a pronounced epistemic spike with only a modest aleatoric increase. In contrast, VRNN and DSSM respond primarily by inflating aleatoric variance with comparatively little epistemic increase, effectively treating the event as observation noise rather than explicit model mismatch. Across all methods, uncertainty returns to baseline within one time step, consistent with a shared isolated data anomaly rather than persistent overconfidence or long-term instability; from a filtering perspective, the LT variants (particularly LT-Unstructured) are therefore well suited for innovation-based gating or reset mechanisms, since anomalous events are expressed *entirely* through epistemic uncertainty rather than being masked by variance inflation.

Summary. Across all evaluations, LT demonstrates stronger sustained per-step performance and improved temporal robustness compared to all baselines. The structured and unstructured variants occupy complementary points on a stability–accuracy tradeoff, while both retain well-behaved and calibrated uncertainty. These gains are achieved despite deliberately lightweight latent inference components, supporting the hypothesis that modeling function evolution via latent-conditioned weight generation is a more effective allocation of capacity than increasing the expressivity of latent inference mechanisms alone.

5. Related Work

Deep state–space and variational sequence models. LT is related to deep state–space models that learn latent dynamics for sequential data, including the Deep Kalman Filter (DKF) (Krishnan et al., 2015), the Deep Variational Bayes Filter (DVBF) (Karl et al., 2017), and the Variational Recurrent Neural Network (VRNN) family (Chung et al., 2015; Fraccaro et al., 2016). These approaches perform filtering in a latent space that directly governs observations. In contrast, LT performs filtering in *function space*: the latent variable generates the parameters of a predictive model rather than the observations themselves, enabling temporally coherent uncertainty over functions with constant-time online updates.

Hypernetworks and weight–space inference. Hypernetworks and weight-generation methods (Ha et al., 2016; Krueger et al., 2017; Pawlowski et al., 2017) treat model parameters as outputs of a secondary network, supporting

amortized Bayesian inference in weight space. LT extends these ideas to sequential settings by evolving the latent variable through time, inducing smooth weight trajectories. This connects hypernetwork-based inference with classical Bayesian filtering ideas such as ensemble Kalman and particle filters, while remaining fully differentiable and end-to-end trainable.

Online and continual learning. Prior work on online adaptation typically relies on gradient-based meta-learning (Finn et al., 2017; Al-Shedivat et al., 2018; Nagabandi et al., 2018), replay buffers (Lopez-Paz & Ranzato, 2017; Chaudhry et al., 2019), or parameter regularization (Kirkpatrick et al., 2017; Zenke et al., 2017). LT instead performs amortized, gradient-free adaptation at each time step via latent filtering, enabling causal updates with constant test-time cost and without catastrophic forgetting. This is related to amortized continual inference (Osterlund et al., 2022), but operates explicitly in weight space rather than activation space.

Function-space inference and temporal forecasting. Gaussian processes and Neural Processes (Garnelo et al., 2018; Kim et al., 2019) perform Bayesian inference over functions, while temporal forecasting models such as DeepAR (Rangapuram et al., 2018a), Deep State Space Models (DSSM) (Doersch et al., 2019), and probabilistic transformers (Gasthaus et al., 2020) predict distributions over future observations. Recent work on Function Distribution Networks (FDNs) (Haq, 2025) similarly performs amortized inference in function space by learning distributions over network weights for static prediction tasks. LT can be viewed as a sequential, parametric analogue that tracks a trajectory of function generators, yielding calibrated predictive mixtures with fixed per-step update cost in non-stationary streams.

Summary. LT lies at the intersection of deep state-space modeling, hypernetwork-based weight generation, and amortized Bayesian filtering, distinguished by moving the filtering operation from data space to function space.

6. Discussion and Limitations

LT reflects a deliberate allocation of model capacity: rather than increasing the expressivity of latent inference components such as the prior, posterior, or transition heads, most capacity is placed in a hypernetwork that generates predictive functions conditioned on a latent state. Consequently, LT employs substantially lighter latent inference components—in our implementation, simple linear heads—than stateful baselines such as VRNN and DSSM, which rely on more expressive nonlinear latent dynamics to compensate for fixed predictors. Despite this asymmetry, and despite static baselines receiving substantially more frequent parameter updates via overlapping windows, LT achieves

stronger sustained performance, suggesting that modeling nonstationarity directly in function space is a more effective and stable use of capacity for long-horizon online prediction.

An important consideration in interpreting these results is the presence of an isolated extreme observation that induces a sharp, synchronized degradation across all evaluated models. In this case, catastrophic deviations in predictive error and likelihood occur simultaneously for stateful and static baselines alike, indicating sensitivity to a shared data anomaly rather than a model-specific failure mode. Notably, the more pronounced response exhibited by LT at this anomaly is consistent with its lower typical error elsewhere and may be advantageous in practice, as sharper excursions facilitate reliable detection and gating of extreme events. Such mitigation mechanisms are standard in filtering systems and are orthogonal to the core architectural contribution, which governs sustained per-step behavior over long horizons.

Finally, LT inherits the parameter scaling behavior of hypernetwork-based models, as increasing predictor or conditioning capacity increases the total parameter count. In practical deployments, this limitation can be mitigated by using LT as an adaptive prediction head on top of a fixed or pretrained backbone, preserving online adaptability while concentrating most capacity in shared representations.

7. Conclusion

LT introduces a predict–generate–update filtering framework in function space, enabling constant-time online adaptation under nonstationary data streams. By conditioning predictive functions on a latent state rather than directly evolving high-capacity latent dynamics, the model achieves superior sustained predictive performance and temporal robustness despite deliberately lightweight latent inference components. Empirical results on long-horizon benchmarks demonstrate consistently lower negative log-likelihood and mean squared error, with competitive calibration, relative to both stateful and static baselines. Together, these findings indicate that function-space adaptation provides a principled and effective alternative to traditional latent-state modeling for online probabilistic prediction under distribution shift.

Impact Statement

This paper presents work whose goal is to advance the field of Machine Learning. There are many potential societal consequences of our work, none of which we feel must be specifically highlighted here.

References

Al-Shedivat, M., Bansal, T., Burda, Y., Sutskever, I., Mordatch, I., and Abbeel, P. Continuous adaptation via meta-learning in nonstationary and competitive environments. In *International Conference on Learning Representations*, 2018.

Blundell, C., Cornebise, J., Kavukcuoglu, K., and Wierstra, D. Weight uncertainty in neural networks. In *Proceedings of the 32nd International Conference on Machine Learning (ICML)*, pp. 1613–1622. PMLR, 2015.

Chaudhry, A., Ranzato, M., Rohrbach, M., and Elhoseiny, M. Continual learning with tiny episodic memories. In *Advances in Neural Information Processing Systems*, 2019.

Chung, J., Kastner, K., Dinh, L., Goel, K., Courville, A., and Bengio, Y. A recurrent latent variable model for sequential data. In *Advances in Neural Information Processing Systems*, 2015.

Doerr, A., Daniel, C., Schiegg, M., Nguyen-Tuong, D., Schaal, S., Toussaint, M., and Trimpe, S. Probabilistic recurrent state-space models. In Dy, J. and Krause, A. (eds.), *Proceedings of the 35th International Conference on Machine Learning*, volume 80 of *Proceedings of Machine Learning Research*, pp. 1280–1289, Stockholm, Sweden, 2018. PMLR. URL <https://proceedings.mlr.press/v80/doerr18a.html>.

Doersch, C., Zoran, D., Garnelo, M., Eslami, S. M. A., Rezende, D. J., Botvinick, M., Osindero, S., and Gregor, K. Cold fusion: Training seq2seq models together with language models. In *International Conference on Learning Representations*, 2019.

Finn, C., Abbeel, P., and Levine, S. Model-agnostic meta-learning for fast adaptation of deep networks. In *International Conference on Machine Learning*, 2017.

Fraccaro, M., Sønderby, S. K., Paquet, U., and Winther, O. Sequential neural models with stochastic layers. In *Advances in Neural Information Processing Systems*, 2016.

Gal, Y. and Ghahramani, Z. Dropout as a bayesian approximation: Representing model uncertainty in deep learning. In *Proceedings of the 33rd International Conference on Machine Learning (ICML)*, pp. 1050–1059. PMLR, 2016.

Garnelo, M., Rosenbaum, D., Maddison, C., Ramalho, T., Saxton, D., Shanahan, M., Teh, Y. W., Rezende, D., and Eslami, S. M. A. Neural processes. In *International Conference on Machine Learning*, 2018.

Gasthaus, J., Benidis, K., Wang, Y., Bohlke-Schneider, M., Flunkert, V., Salinas, D., Januschowski, T., Maddix, D., Rangapuram, S. S., and Kurle, R. Probabilistic transformer: Modelling time series with distributions. In *Advances in Neural Information Processing Systems*, 2020.

Ha, D., Dai, A., and Le, Q. V. Hypernetworks. *arXiv preprint arXiv:1609.09106*, 2016.

Haq, O. Function distribution networks. *arXiv preprint arXiv:2510.17794*, 2025.

Karl, M., Soelch, M., Bayer, J., and van der Smagt, P. Deep variational bayes filters: Unsupervised learning of state space models from raw data. In *International Conference on Learning Representations*, 2017.

Kim, H., Mnih, A., Schwarz, J., Garnelo, M., Eslami, S. M. A., Rosenbaum, D., Vinyals, O., and Teh, Y. W. Attentive neural processes. In *International Conference on Learning Representations*, 2019.

Kirkpatrick, J., Pascanu, R., Rabinowitz, N., Veness, J., et al. Overcoming catastrophic forgetting in neural networks. In *Proceedings of the National Academy of Sciences*, 2017.

Krishnan, R. G., Shalit, U., and Sontag, D. Deep kalman filters. In *Proceedings of the 31st Conference on Uncertainty in Artificial Intelligence*, 2015.

Krueger, D., Huang, C., Islam, R., Turner, R., and Lacoste, A. Bayesian hypernetworks. In *International Conference on Learning Representations*, 2017.

Lakshminarayanan, B., Pritzel, A., and Blundell, C. Simple and scalable predictive uncertainty estimation using deep ensembles. In *Advances in Neural Information Processing Systems (NeurIPS)*, pp. 6402–6413, 2017.

Lopez-Paz, D. and Ranzato, M. Gradient episodic memory for continual learning. In *Advances in Neural Information Processing Systems*, 2017.

Nagabandi, A., Finn, C., and Levine, S. Learning to adapt in dynamic, real-world environments through meta-reinforcement learning. In *International Conference on Learning Representations*, 2018.

Osterlund, E., Zoubin, G., and Turner, R. Continual inference: A neural architecture for online bayesian inference. *arXiv preprint arXiv:2203.14209*, 2022.

Pawlowski, N., Brock, A., Lee, J., Rajchl, M., and Glocker, B. Implicit weight uncertainty in neural networks. In *International Conference on Learning Representations*, 2017.

Rangapuram, S. S., Seeger, M. W., Gasthaus, J., Stella, L., Wang, Y., and Januschowski, T. Deepar: Probabilistic forecasting with autoregressive recurrent networks. In *International Journal of Forecasting*, 2018a.

Rangapuram, S. S., Seeger, M. W., Gasthaus, J.,
Stella, L., Wang, Y., and Januschowski, T. Deep
state space models for time series forecasting. In
Advances in Neural Information Processing Systems, volume 31. Curran Associates, Inc., 2018b.
URL <https://papers.nips.cc/paper/8004-deep-state-space-models-for-time-series-forecasting>.

Zenke, F., Poole, B., and Ganguli, S. Continual learning
through synaptic intelligence. In *International Conference on Machine Learning*, 2017.

A. Deriving the Looser Structured ELBO

From the prior predictive to an explicit transition.

$$p(\mathcal{D}_t \mid \mathcal{D}_{1:t-1}) = \int p(\mathcal{D}_t \mid z_t) p_\phi(z_t \mid \mathcal{D}_{1:t-1}) dz_t, \quad (8)$$

with Chapman–Kolmogorov (CK)

$$p_\phi(z_t \mid \mathcal{D}_{1:t-1}) = \int p_\phi(z_t \mid z_{t-1}, \mathcal{D}_{1:t-1}) p_\phi(z_{t-1} \mid \mathcal{D}_{1:t-1}) dz_{t-1}. \quad (9)$$

Standard filtering ELBO. Using $q_\psi(z_t \mid \mathcal{D}_{1:t})$,

$$\begin{aligned} \log p(\mathcal{D}_t \mid \mathcal{D}_{1:t-1}) &\geq \mathbb{E}_{q_\psi(z_t \mid \mathcal{D}_{1:t})} [\log p(\mathcal{D}_t \mid z_t)] \\ &\quad - \text{KL}\left(q_\psi(z_t \mid \mathcal{D}_{1:t}) \parallel p_\phi(z_t \mid \mathcal{D}_{1:t-1})\right). \end{aligned} \quad (10)$$

Expand the KL as an integral (keep $q \log q$ intact).

$$\text{KL}\left(q_\psi \parallel p_\phi(\cdot \mid \mathcal{D}_{1:t-1})\right) = \int q_\psi(z_t \mid \mathcal{D}_{1:t}) \left[\underbrace{\log q_\psi(z_t \mid \mathcal{D}_{1:t})}_{q \log q \text{ (unchanged)}} - \log p_\phi(z_t \mid \mathcal{D}_{1:t-1}) \right] dz_t. \quad (11)$$

Insert CK into the $-\log$ term and apply Jensen (log-sum). Substitute (9) into the $-\log$ term of (11):

$$-\log p_\phi(z_t \mid \mathcal{D}_{1:t-1}) = -\log \int p_\phi(z_t \mid z_{t-1}, \mathcal{D}_{1:t-1}) p_\phi(z_{t-1} \mid \mathcal{D}_{1:t-1}) dz_{t-1}.$$

By concavity of \log (log-sum inequality), for each fixed z_t ,

$$-\log \int p_\phi(z_t \mid z_{t-1}, \mathcal{D}_{1:t-1}) p_\phi(z_{t-1} \mid \mathcal{D}_{1:t-1}) dz_{t-1} \leq -\int p_\phi(z_{t-1} \mid \mathcal{D}_{1:t-1}) \log p_\phi(z_t \mid z_{t-1}, \mathcal{D}_{1:t-1}) dz_{t-1}.$$

Plugging this *only* into the second term of (11) yields

$$\begin{aligned} \text{KL}\left(q_\psi \parallel p_\phi(\cdot \mid \mathcal{D}_{1:t-1})\right) &\leq \int q_\psi(z_t \mid \mathcal{D}_{1:t}) \left[\log q_\psi(z_t \mid \mathcal{D}_{1:t}) - \int p_\phi(z_{t-1} \mid \mathcal{D}_{1:t-1}) \log p_\phi(z_t \mid z_{t-1}, \mathcal{D}_{1:t-1}) dz_{t-1} \right] dz_t \\ &= \int p_\phi(z_{t-1} \mid \mathcal{D}_{1:t-1}) \left(\int q_\psi(z_t \mid \mathcal{D}_{1:t}) \left[\log q_\psi(z_t \mid \mathcal{D}_{1:t}) - \log p_\phi(z_t \mid z_{t-1}, \mathcal{D}_{1:t-1}) \right] dz_t \right) dz_{t-1} \\ &= \mathbb{E}_{p_\phi(z_{t-1} \mid \mathcal{D}_{1:t-1})} [\text{KL}(q_\psi(z_t \mid \mathcal{D}_{1:t}) \parallel p_\phi(z_t \mid z_{t-1}, \mathcal{D}_{1:t-1}))]. \end{aligned} \quad (12)$$

(Interchanging integrals above is justified by Fubini/Tonelli.)

Structured ELBO (looser). Substitute (12) into (10):

$$\mathcal{L}_t^{\text{struct}} = \mathbb{E}_{q_\psi(z_t \mid \mathcal{D}_{1:t})} [\log p(\mathcal{D}_t \mid z_t)] - \mathbb{E}_{p_\phi(z_{t-1} \mid \mathcal{D}_{1:t-1})} [\text{KL}(q_\psi(z_t \mid \mathcal{D}_{1:t}) \parallel p_\phi(z_t \mid z_{t-1}, \mathcal{D}_{1:t-1}))], \quad (13)$$

and thus $\mathcal{L}_t^{\text{struct}} \leq \mathcal{L}_t$.

Practical amortization. Replace the intractable outer expectation by the previous amortized filter:

$$\mathcal{L}_t^{\text{struct}} \approx \mathbb{E}_{q_\psi(z_t \mid \mathcal{D}_{1:t})} [\log p(\mathcal{D}_t \mid z_t)] - \mathbb{E}_{q_\psi(z_{t-1} \mid \mathcal{D}_{1:t-1})} [\text{KL}(q_\psi(z_t \mid \mathcal{D}_{1:t}) \parallel p_\phi(z_t \mid z_{t-1}, \mathcal{D}_{1:t-1}))]. \quad (14)$$

Interpretation. The $q \log q$ term remains unchanged; the looseness comes solely from bounding

$$-\log \int p_\phi(z_t \mid z_{t-1}, \mathcal{D}_{1:t-1}) p_\phi(z_{t-1} \mid \mathcal{D}_{1:t-1}) dz_{t-1} \leq -\int p_\phi(z_{t-1} \mid \mathcal{D}_{1:t-1}) \log p_\phi(z_t \mid z_{t-1}, \mathcal{D}_{1:t-1}) dz_{t-1}.$$

This converts the prior KL into an *expected* KL to the transition, promoting temporal coherence at the cost of a looser bound.

B. Online Training Algorithm

This appendix describes the online training and inference procedures used for all stateful models evaluated in this work. All models optimize an online variational objective over a streaming sequence and differ only in how temporal dependencies are handled during training, specifically in how gradients are accumulated, how latent states are detached, and how credit is assigned across time. Inference is performed causally and without gradients for all methods.

All main experimental results use a single training configuration: *chunked truncated backpropagation through time (TBPTT)* with *fixed recency weighting*. This choice provides a stable and computationally efficient trade-off between temporal credit assignment and memory cost, and is applied uniformly across all stateful baselines for fairness. Other training schedules are included below for completeness and to clarify the design space, but are not used in the reported results.

In chunked TBPTT, the model processes the data stream sequentially while accumulating a credit-weighted sum of per-step ELBOs over a finite window of length W . At window boundaries, a single optimizer update is performed and the recurrent state is detached to prevent gradients from propagating indefinitely backward in time. This enforces a bounded temporal horizon while preserving causal training.

Within each window, per-step losses are combined using a *fixed recency* weighting scheme, $w_\tau = \lambda^{t-\tau}$ where $\lambda \in (0, 1]$, which exponentially downweights older time steps and prioritizes recent observations. The resulting weighted objective is normalized before backpropagation to ensure scale invariance across windows. This simple causal weighting was found to be stable and effective in practice and is used throughout the paper. We additionally implement a *surprise-aware* variant that modulates the recency weights according to $w_\tau = \lambda^{t-\tau} \cdot \exp(\alpha [\text{NLL}_\tau - \text{EMA_NLL}_\tau]_+)$, where $[\cdot]_+ = \max(\cdot, 0)$ and EMA_NLL_τ denotes an exponential moving average of recent negative log-likelihood values. This mechanism increases credit on unexpectedly high-error steps while preserving causality. It is included for completeness but is not used in the reported experiments. Pseudocode for all training and inference variants is provided below.

Algorithm 1 LT (training): Exact rolling-window

```

1: Inputs: window  $W$ , update stride  $S$ , weights  $w_\tau > 0$  (fixed recency or surprise-aware, detached), KL schedule  $\beta_t$ , mixture samples  $K$ 
2: Init summary  $h_0$ ; params  $\phi, \psi, \eta, \vartheta$ ; prior  $p_\phi(z_1)$ . // keep ring buffer of recent  $\mathcal{D}_\tau$  and detached  $s_\tau$ 
3: for  $t = 1$  to  $T$  do
4:   Advance stream (no graph kept):
5:    $(x_t, y_t) \leftarrow \mathcal{D}_t$ ;  $e_t = \text{Enc}_\psi(\mathcal{D}_t)$ ;  $h_t^{\text{det}} = \text{RNN}_\psi(h_{t-1}^{\text{det}}, e_t)$ ; // store  $h_t^{\text{det}} = \text{stop\_grad}(h_t^{\text{det}})$ 
6:   if  $(t \bmod S = 0)$  or  $t = T$  then
7:     Recompute last  $W$  under current params (fresh graph):
8:      $t_{\min} = \max(1, t - W + 1)$ ;  $h \leftarrow h_{t_{\min}-1}^{\text{det}}$ ;  $L_{\text{acc}} \leftarrow 0$ ;  $Z \leftarrow 0$ 
9:     for  $\tau = t_{\min}$  to  $t$  do
10:       $(\mu_\tau^{(p)}, \log \sigma_\tau^{(p)}) = \text{Head}_{p_\phi}(s)$ 
11:       $e_\tau = \text{Enc}_\psi(\mathcal{D}_\tau)$ ;  $s = \text{RNN}_\psi(s, e_\tau)$ 
12:       $(\mu_\tau^{(q)}, \log \sigma_\tau^{(q)}) = \text{Head}_{q_\psi}(s)$ 
13:      Sample  $z_\tau^{(k)} \sim \mathcal{N}(\mu_\tau^{(q)}, \text{diag}(\sigma_\tau^{(q)2}))$ ,  $k = 1..K$ ;  $\theta_\tau^{(k)} = g_\eta(z_\tau^{(k)})$ 
14:       $\widehat{\mathbb{E}} \log p_\tau = \frac{1}{K} \sum_k \log p_\vartheta(y_\tau \mid x_\tau; \theta_\tau^{(k)})$ 
15:       $KL_\tau = \text{KL}(\mathcal{N}(\mu_\tau^{(q)}, \sigma_\tau^{(q)2}) \parallel \mathcal{N}(\mu_\tau^{(p)}, \sigma_\tau^{(p)2}))$  (structured: replace by  $\mathbb{E}_{q_\psi(z_{\tau-1} \mid \mathcal{D}_{1:\tau-1})} [\text{KL}(q_\psi(z_\tau \mid \cdot) \parallel p_\phi(z_\tau \mid z_{\tau-1}, \cdot))]$ ; see App.)
16:       $\mathcal{L}_\tau = \widehat{\mathbb{E}} \log p_\tau - \beta_\tau KL_\tau$ 
17:      Credit weight: set  $w_\tau$  (fixed recency or surprise-aware), then  $w_\tau \leftarrow \text{stop\_grad}(w_\tau)$ ;  $L_{\text{acc}} += w_\tau \mathcal{L}_\tau$ ;  $Z += w_\tau$ 
18:    end for
19:    Backprop & step: loss =  $L_{\text{acc}} / \max(Z, \varepsilon)$ ; opt.zero_grad(); loss.backward(); opt.step()
20:    (optional) detach checkpoint: set  $h_t^{\text{det}} \leftarrow \text{stop\_grad}(h_t)$  // keeps a clean checkpoint for future recomputes
21:  end if
22: end for

```

Algorithm 2 LT (training): **Chunk stride** (partial-window updates with TBPTT)

```

1: Inputs: window  $W$ , weights  $w_\tau > 0$  (fixed recency or surprise-aware, detached), KL schedule  $\beta_t$ , mixture samples  $K$ 
2: Init  $h_0$ ; params  $\phi, \psi, \eta, \vartheta$ ; prior  $p_\phi(z_1)$ 
3:  $L_{\text{acc}} \leftarrow 0$ ;  $Z \leftarrow 0$ 
4: for  $t = 1$  to  $T$  do
5:    $(\mu_t^{(p)}, \log \sigma_t^{(p)}) = \text{Head}_{p_\phi}(h_{t-1})$ 
6:    $(x_t, y_t) \leftarrow \mathcal{D}_t$ ;  $e_t = \text{Enc}_\psi(\mathcal{D}_t)$ ;  $h_t = \text{RNN}_\psi(h_{t-1}, e_t)$ 
7:    $(\mu_t^{(q)}, \log \sigma_t^{(q)}) = \text{Head}_{q_\psi}(h_t)$ 
8:   Sample  $z_t^{(k)}$ ;  $\theta_t^{(k)} = g_\eta(z_t^{(k)})$ 
9:    $\widehat{\mathbb{E}} \log p_t = \frac{1}{K} \sum_k \log p_\vartheta(y_t | x_t; \theta_t^{(k)})$ 
10:   $KL_t = \text{KL}(\mathcal{N}(\mu_t^{(q)}, \sigma_t^{(q)2}) \parallel \mathcal{N}(\mu_t^{(p)}, \sigma_t^{(p)2}))$  (structured: same replacement as Exact; see App.)
11:   $\mathcal{L}_t = \widehat{\mathbb{E}} \log p_t - \beta_t KL_t$ 
12:  Credit weight: choose  $w_t$  (fixed recency or surprise-aware), then  $w_t \leftarrow \text{stop\_grad}(w_t)$ ;  $L_{\text{acc}} += w_t \mathcal{L}_t$ ;  $Z += w_t$ 
13:  if  $(t - t_0 + 1) \bmod W = 0$  then
14:    Stride update on partial chunk: loss =  $L_{\text{acc}} / \max(Z, \varepsilon)$ ; step optimizer; reset  $L_{\text{acc}}, Z$ ;  $h_t \leftarrow \text{stop\_grad}(h_t)$ 
15:  end if
16: end for

```

Algorithm 3 LT (training): **Approx stride** micro-steps + window-end TBPTT

```

1: Inputs: window  $W$ , stride  $S$ , weights  $w_\tau > 0$  (fixed recency or surprise-aware, detached), KL schedule  $\beta_t$ , mixture samples  $K$ 
2: Init  $h_0$ ; params  $\phi, \psi, \eta, \vartheta$ ; prior  $p_\phi(z_1)$ 
3:  $t_0 \leftarrow 1$ 
4: for  $t = 1$  to  $T$  do
5:   if  $t = t_0$  then
6:      $h_{t-1} \leftarrow \text{stop\_grad}(h_{t-1})$ 
7:   end if
8:    $(\mu_t^{(p)}, \log \sigma_t^{(p)}) = \text{Head}_{p_\phi}(h_{t-1})$ 
9:    $(x_t, y_t) \leftarrow \mathcal{D}_t$ ;  $e_t = \text{Enc}_\psi(\mathcal{D}_t)$ ;  $h_t = \text{RNN}_\psi(h_{t-1}, e_t)$ 
10:   $(\mu_t^{(q)}, \log \sigma_t^{(q)}) = \text{Head}_{q_\psi}(h_t)$ 
11:  Sample  $z_t^{(k)}$ ;  $\theta_t^{(k)} = g_\eta(z_t^{(k)})$ 
12:   $\widehat{\mathbb{E}} \log p_t = \frac{1}{K} \sum_k \log p_\vartheta(y_t | x_t; \theta_t^{(k)})$ 
13:   $KL_t = \text{KL}(\mathcal{N}(\mu_t^{(q)}, \sigma_t^{(q)2}) \parallel \mathcal{N}(\mu_t^{(p)}, \sigma_t^{(p)2}))$  (structured: same replacement as Exact; see App.)
14:   $\mathcal{L}_t = \widehat{\mathbb{E}} \log p_t - \beta_t KL_t$ 
15:  if  $(t - t_0 + 1) \bmod S = 0$  and  $(t - t_0 + 1) < W$  then
16:    Micro-step (short horizon): treat  $h_{t-1}$  as detached just for this step; step optimizer on  $\mathcal{L}_t$ 
17:  end if
18:  if  $((t - t_0 + 1) = W)$  or  $t = T$  then
19:    Recompute last  $W$  under current params (fresh graph for TBPTT):
20:       $t_{\min} = \max(1, t - W + 1)$ ;  $L_{\text{acc}} \leftarrow 0$ ;  $Z \leftarrow 0$ ;  $h \leftarrow h_{t_{\min}-1}$  (detached)
21:      for  $\tau = t_{\min}$  to  $t$  do
22:        // repeat the per-step block to rebuild  $\mathcal{L}_\tau$  (sample with  $K$ , compute KL and  $\mathcal{L}_\tau$  as above)
23:        Credit weight: set  $w_\tau$  (fixed recency or surprise-aware, detached)
24:         $L_{\text{acc}} += w_\tau \mathcal{L}_\tau$ ;  $Z += w_\tau$ 
25:      end for
26:      Window-end TBPTT: loss =  $L_{\text{acc}} / \max(Z, \varepsilon)$ ; step optimizer
27:       $h_t \leftarrow \text{stop\_grad}(h_t)$ ;  $t_0 \leftarrow t + 1$ 
28:  end if
29: end for

```

Algorithm 4 LT (inference): streaming prediction without gradients

- 1: Carry forward summary h_{t-1}
- 2: **Predict (prior):** $(\mu_t^{(p)}, \log \sigma_t^{(p)}) = \text{Head}_{p_\phi}(h_{t-1})$
- 3: **Produce prediction (known covariates):** for $k = 1..K$, sample $z_t^{(k)} \sim \mathcal{N}(\mu_t^{(p)}, \text{diag}(\sigma_t^{(p)2}))$; set $\theta_t^{(k)} = g_\eta(z_t^{(k)})$; output mixture $\hat{p}(y_t | x_t, \mathcal{D}_{1:t-1}) \approx \frac{1}{K} \sum_k p_\phi(y_t | x_t; \theta_t^{(k)})$
- 4: **Receive $\mathcal{D}_t = (x_t, y_t)$ and update state (no gradients):** encode $\mathcal{D}_t \rightarrow e_t$; $h_t = \text{RNN}(h_{t-1}, e_t)$

C. VRNN and DSSM baselines

We model a sequence of inputs and targets $\{(x_t, y_t)\}_{t=1}^T$ with latent-variable recurrent baselines. Both methods define a conditional model $p_\theta(y_{1:T} | x_{1:T})$ via per-step latent variables z_t and a deterministic recurrent state h_t . They differ primarily in *where* the latent z_t enters the dynamics.

Throughout, we assume diagonal Gaussians $\mathcal{N}(\mu, \Sigma)$ with $\Sigma = \text{diag}(\sigma^2)$, and write $\text{KL}(\cdot \| \cdot)$ for the KL between diagonal Gaussians.

C.1. VRNN baseline

Our VRNN baseline follows the structure of [Chung et al. \(2015\)](#), adapted to conditional regression. Let $h_t \in \mathbb{R}^{d_h}$ denote a deterministic RNN state and $z_t \in \mathbb{R}^{d_z}$ a stochastic latent. We parameterize the model with neural networks prior_θ , dec_θ , ϕ_x and ϕ_z , and a GRU cell f_θ .

Deterministic state. We initialize $h_0 = 0$ and update

$$h_t = f_\theta(h_{t-1}, \phi_x(x_t), \phi_z(z_t)), \quad (15)$$

i.e., the RNN state depends on both the current input and the sampled latent.

Latent prior and likelihood. Conditioned on h_{t-1} , the prior over z_t is

$$p_\theta(z_t | h_{t-1}) = \mathcal{N}(z_t; \mu_t^p, \text{diag}((\sigma_t^p)^2)), \quad [\mu_t^p, \log(\sigma_t^p)^2] = \text{prior}_\theta(h_{t-1}). \quad (16)$$

Given x_t , z_t , and h_t , the emission model is

$$p_\theta(y_t | x_t, z_t, h_t) = \mathcal{N}(y_t; \mu_t^y, \text{diag}((\sigma_t^y)^2)), \quad [\mu_t^y, \log(\sigma_t^y)^2] = \text{dec}_\theta([h_t, z_t, x_t]). \quad (17)$$

Variational posterior. For training we introduce a per-step amortized posterior

$$q_\phi(z_t | x_t, y_t, h_{t-1}) = \mathcal{N}(z_t; \mu_t^q, \text{diag}((\sigma_t^q)^2)), \quad [\mu_t^q, \log(\sigma_t^q)^2] = \text{enc}_\phi([h_{t-1}, x_t, y_t]). \quad (18)$$

Sampling uses the standard reparameterization $z_t = \mu_t^q + \sigma_t^q \odot \varepsilon_t$ with $\varepsilon_t \sim \mathcal{N}(0, I)$.

Conditional joint (derivation). Fix $x_{1:T}$ and introduce the full joint over $(y_{1:T}, z_{1:T}, h_{1:T})$. Using the chain rule at each time step with the ordering $z_t \rightarrow h_t \rightarrow y_t$ gives

$$p_\theta(y_{1:T}, z_{1:T}, h_{1:T} | x_{1:T}) = \prod_{t=1}^T p_\theta(z_t | y_{1:t-1}, z_{1:t-1}, h_{1:t-1}, x_{1:T}) p_\theta(h_t | y_{1:t-1}, z_{1:t}, h_{1:t-1}, x_{1:T}) p_\theta(y_t | y_{1:t-1}, z_{1:t}, h_{1:t}, x_{1:T}). \quad (19)$$

We now impose the VRNN conditional independences implied by Equations (15) to (17):

$$p_\theta(z_t | y_{1:t-1}, z_{1:t-1}, h_{1:t-1}, x_{1:T}) = p_\theta(z_t | h_{t-1}), \quad (20)$$

$$p_\theta(h_t | y_{1:t-1}, z_{1:t}, h_{1:t-1}, x_{1:T}) = \delta(h_t - f_\theta(h_{t-1}, \phi_x(x_t), \phi_z(z_t))), \quad (21)$$

$$p_\theta(y_t | y_{1:t-1}, z_{1:t}, h_{1:t}, x_{1:T}) = p_\theta(y_t | x_t, z_t, h_t), \quad (22)$$

where $\delta(\cdot)$ is the Dirac delta. Substituting Equations (20) to (22) into Equation (19) yields

$$p_\theta(y_{1:T}, z_{1:T}, h_{1:T} | x_{1:T}) = \prod_{t=1}^T p_\theta(z_t | h_{t-1}) \delta(h_t - f_\theta(h_{t-1}, \phi_x(x_t), \phi_z(z_t))) p_\theta(y_t | x_t, z_t, h_t). \quad (23)$$

Integrating out the deterministic states $h_{1:T}$ gives the conditional joint over $(y_{1:T}, z_{1:T})$:

$$\begin{aligned} p_\theta(y_{1:T}, z_{1:T} | x_{1:T}) &= \int p_\theta(y_{1:T}, z_{1:T}, h_{1:T} | x_{1:T}) dh_{1:T} \\ &= \prod_{t=1}^T p_\theta(z_t | h_{t-1}) p_\theta(y_t | x_t, z_t, h_t), \end{aligned} \quad (24)$$

where $h_t = f_\theta(h_{t-1}, \phi_x(x_t), \phi_z(z_t))$ is the deterministic RNN state from Equation (15).

ELBO (derivation). We optimize the conditional log-likelihood $\log p_\theta(y_{1:T} | x_{1:T})$ via a variational lower bound. Using Equation (24),

$$\begin{aligned} \log p_\theta(y_{1:T} | x_{1:T}) &= \log \int p_\theta(y_{1:T}, z_{1:T} | x_{1:T}) dz_{1:T} \\ &= \log \int q_\phi(z_{1:T} | x_{1:T}, y_{1:T}) \frac{p_\theta(y_{1:T}, z_{1:T} | x_{1:T})}{q_\phi(z_{1:T} | x_{1:T}, y_{1:T})} dz_{1:T} \\ &\geq \mathbb{E}_{q_\phi(z_{1:T} | x_{1:T}, y_{1:T})} \left[\log p_\theta(y_{1:T}, z_{1:T} | x_{1:T}) - \log q_\phi(z_{1:T} | x_{1:T}, y_{1:T}) \right], \end{aligned} \quad (25)$$

where the inequality is Jensen's inequality. We now assume a mean-field factorization $q_\phi(z_{1:T} | x_{1:T}, y_{1:T}) = \prod_{t=1}^T q_\phi(z_t | x_t, y_t, h_{t-1})$ and plug in Equation (24):

$$\begin{aligned} \mathbb{E}_{q_\phi} \left[\log p_\theta(y_{1:T}, z_{1:T} | x_{1:T}) \right] &= \mathbb{E}_{q_\phi} \left[\sum_{t=1}^T \left(\log p_\theta(z_t | h_{t-1}) + \log p_\theta(y_t | x_t, z_t, h_t) \right) \right] \\ &= \sum_{t=1}^T \mathbb{E}_{q_\phi(z_t | x_t, y_t, h_{t-1})} \left[\log p_\theta(y_t | x_t, z_t, h_t) \right] \\ &\quad + \sum_{t=1}^T \mathbb{E}_{q_\phi(z_t | x_t, y_t, h_{t-1})} \left[\log p_\theta(z_t | h_{t-1}) \right], \end{aligned} \quad (26)$$

and similarly

$$\mathbb{E}_{q_\phi} \left[\log q_\phi(z_{1:T} | x_{1:T}, y_{1:T}) \right] = \sum_{t=1}^T \mathbb{E}_{q_\phi(z_t | x_t, y_t, h_{t-1})} \left[\log q_\phi(z_t | x_t, y_t, h_{t-1}) \right]. \quad (27)$$

Substituting Equations (26) and (27) into Equation (25) yields

$$\begin{aligned} \log p_\theta(y_{1:T} | x_{1:T}) &\geq \sum_{t=1}^T \mathbb{E}_{q_\phi(z_t | x_t, y_t, h_{t-1})} \left[\log p_\theta(y_t | x_t, z_t, h_t) \right] \\ &\quad + \sum_{t=1}^T \mathbb{E}_{q_\phi(z_t | x_t, y_t, h_{t-1})} \left[\log p_\theta(z_t | h_{t-1}) - \log q_\phi(z_t | x_t, y_t, h_{t-1}) \right]. \end{aligned} \quad (28)$$

The second sum is $-\sum_t \text{KL}(q_\phi(\cdot) \| p_\theta(\cdot))$, giving the standard VRNN ELBO:

$$\mathcal{L}_{\text{VRNN}} = \sum_{t=1}^T \mathbb{E}_{q_\phi(z_t | x_t, y_t, h_{t-1})} \left[\log p_\theta(y_t | x_t, z_t, h_t) \right] - \sum_{t=1}^T \text{KL} \left(q_\phi(z_t | x_t, y_t, h_{t-1}) \middle\| p_\theta(z_t | h_{t-1}) \right). \quad (29)$$

In the implementation, we use a β -weighted KL, $\mathcal{L}_{\text{VRNN}}^\beta = \sum_t \mathbb{E}[\log p_\theta(y_t | \cdot)] - \beta \sum_t \text{KL}(\cdot \| \cdot)$, and estimate each term using a single Monte Carlo sample from q_ϕ .

C.2. DSSM baseline

The DSSM baseline follows a deterministic+stochastic state-space model. We maintain a deterministic state h_t that summarizes the observed pair (x_t, y_t) , and attach a stochastic latent z_t that modulates the emission. Unlike VRNN, the latent does not enter the recurrent update.

Deterministic state. We define an encoder ϕ_e over the current pair (x_t, y_t) and a GRU cell:

$$e_t = \phi_e([x_t, y_t]), \quad h_t = f_\theta(h_{t-1}, e_t). \quad (30)$$

We treat h_t as a deterministic summary of all past observations $(x_{1:t}, y_{1:t})$; it is not a random variable in the generative model, but conditions both the prior and decoder.

Latent prior and likelihood. Conditioned on h_{t-1} , the prior over z_t is again diagonal Gaussian:

$$p_\theta(z_t | h_{t-1}) = \mathcal{N}(z_t; \mu_t^p, \text{diag}((\sigma_t^p)^2)), \quad [\mu_t^p, \log(\sigma_t^p)^2] = \text{prior}_\theta(h_{t-1}). \quad (31)$$

Given x_t , z_t , and h_t , the emission is

$$p_\theta(y_t | x_t, z_t, h_t) = \mathcal{N}(y_t; \mu_t^y, \text{diag}((\sigma_t^y)^2)), \quad [\mu_t^y, \log(\sigma_t^y)^2] = \text{dec}_\theta([h_t, z_t, x_t]). \quad (32)$$

Variational posterior. The amortized posterior conditions on both the previous state and the encoded current pair:

$$q_\phi(z_t | x_t, y_t, h_{t-1}) = \mathcal{N}(z_t; \mu_t^q, \text{diag}((\sigma_t^q)^2)), \quad [\mu_t^q, \log(\sigma_t^q)^2] = \text{post}_\phi([h_{t-1}, e_t]). \quad (33)$$

Sampling again uses reparameterization.

Joint and ELBO. For DSSM, the same chain-rule argument as in Equation (19)–Equation (24), with the deterministic update $h_t = f_\theta(h_{t-1}, \phi_e([x_t, y_t]))$ in place of Equation (15), yields the conditional joint

$$p_\theta(y_{1:T}, z_{1:T} | x_{1:T}) = \prod_{t=1}^T p_\theta(z_t | h_{t-1}) p_\theta(y_t | x_t, z_t, h_t), \quad (34)$$

where h_t is the deterministic state from Equation (30). Repeating the variational derivation in Equation (25)–Equation (29) with the factorization $q_\phi(z_{1:T} | x_{1:T}, y_{1:T}) = \prod_t q_\phi(z_t | x_t, y_t, h_{t-1})$ and the definitions in Equations (31) to (33) gives the DSSM ELBO

$$\mathcal{L}_{\text{DSSM}} = \sum_{t=1}^T \mathbb{E}_{q_\phi(z_t | h_{t-1}, x_t, y_t)} \left[\log p_\theta(y_t | x_t, z_t, h_t) \right] - \sum_{t=1}^T \text{KL} \left(q_\phi(z_t | x_t, y_t, h_{t-1}) \middle\| p_\theta(z_t | h_{t-1}) \right). \quad (35)$$

In practice, we again apply a β -weight on the KL and use a single Monte Carlo sample from q_ϕ per step.

C.3. Comparison

Both baselines share the same conditional prior family $p_\theta(z_t | h_{t-1})$ and Gaussian decoder $p_\theta(y_t | x_t, z_t, h_t)$, and are trained with nearly identical one-step ELBOs. The key structural difference lies in the deterministic recurrence:

- **VRNN** uses the latent in the core dynamics (Equation (15)): h_t depends on z_t (via $\phi_z(z_t)$), so information about past latents propagates forward through the RNN state.
- **DSSM** keeps the recurrent state purely observation-driven (Equation (30)): h_t depends on the encoded pair $e_t = \phi_e([x_t, y_t])$ but not on z_t ; the latent z_t only modulates the emission (Equation (32)).

This yields two complementary latent sequence baselines under a matched ELBO objective: VRNN represents a “latent-in-the-dynamics” recurrent model, while DSSM represents a deterministic RNN with an auxiliary latent head on top of its observation-driven state.

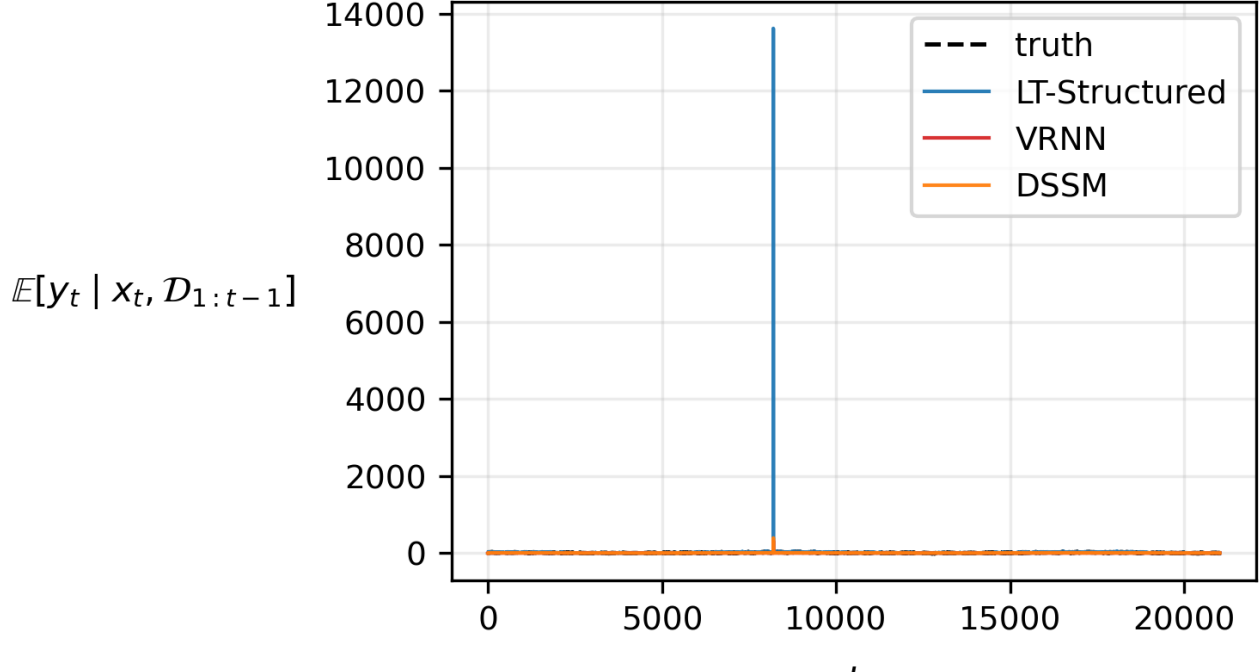
D. Tables and Figures

Table 2. Training protocol, capacity constraints, and optimization settings used across all experiments.

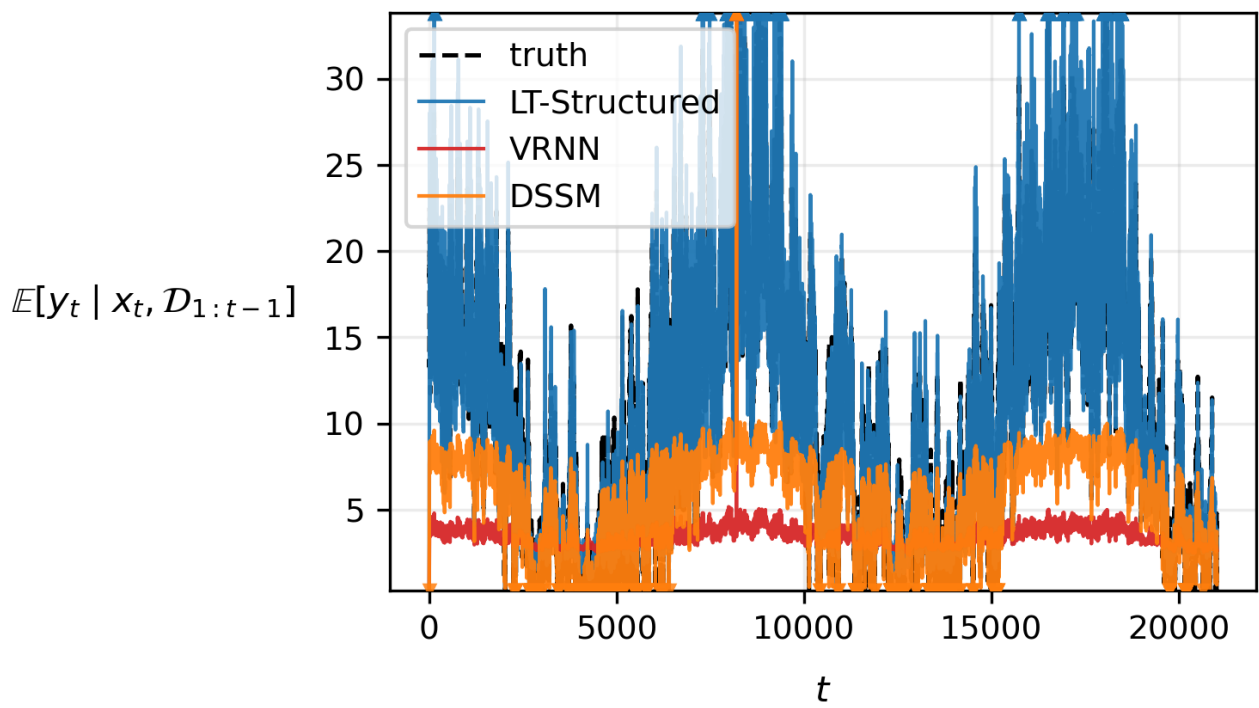
Setting	Value
Dataset	Jena Climate
Train / evaluation split	80% / 20% (chronological)
Epochs	6
Random seeds	25
Stateful models	LT, VRNN, DSSM
Training scheme (stateful)	TBPTT (no overlap)
TBPTT window length W	256
Recency weighting	Fixed, $\lambda = 0.9$
Latent dimension	$\dim(z_t) = 8$
Hidden state dimension	$\dim(h_t) = 64$
Static models	MC-Dropout, BBB, Deep Ensembles
Training scheme (static)	Sliding window
Window length / stride	$W = 256, S = 32$
Relative updates per epoch	$\approx 8 \times$ stateful models
KL annealing schedule	Linear
Maximum β	$\beta_{\max} = 1$
Warmup (stateful)	$\beta_{\text{warmup}} = 575$ updates
Warmup (static)	$\beta_{\text{warmup}} = 4600$ updates
Generated weights (LT)	Entire predictor network
Inference-time parameter budget	20k parameters ($\pm 5\%$)
Total trainable parameters	20k parameters ($\pm 10\%$)
Inference-time sampling	$K = 100$ MC samples
Training-time sampling	$K = 1$ MC sample
Deep Ensemble size	$M = 10$ members
Optimizer	Adam
Learning rate	1×10^{-4}
Gradient clipping	ℓ_2 norm clipped at 1.0

Table 3. Model parameter counts. *Total Parameters* includes all trainable parameters used during training, while *Inference-Time Parameters* reports the number of parameters active at deployment.

Model	Total Parameters	Inference-Time Parameters
Bayes-by-Backprop (BBB)	20,060	20,060
DSSM	22,262	20,630
Deep Ensembles	19,100	19,100
LT (Structured)	20,709	20,709
LT (Unstructured)	21,888	20,848
MC-Dropout	19,112	19,112
VRNN	20,758	20,758



(a) Predictive mean vs t



(b) Predictive mean vs t (clipped)

Figure 5. Predictive mean trajectories for a representative seed. (a) Unclipped predictive mean $\mathbb{E}[y_t | x_t, \mathcal{D}_{1:t-1}]$ over the full time horizon, illustrating a single isolated divergence event for LT-Structured. (b) Clipped view of the same trajectories to highlight typical predictive behavior across methods. The isolated spike in (a) corresponds to a rare catastrophic failure and dominates untrimmed temporal mean statistics, while the clipped view in (b) shows that LT-Structured otherwise tracks the signal accurately over time.

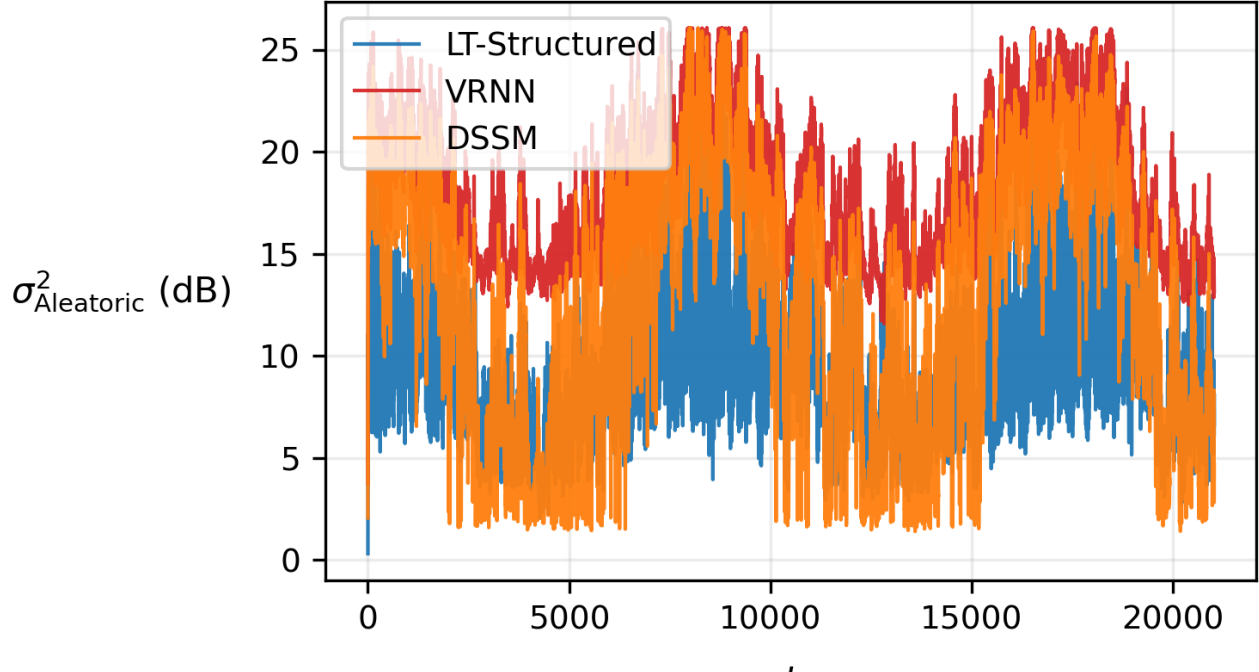
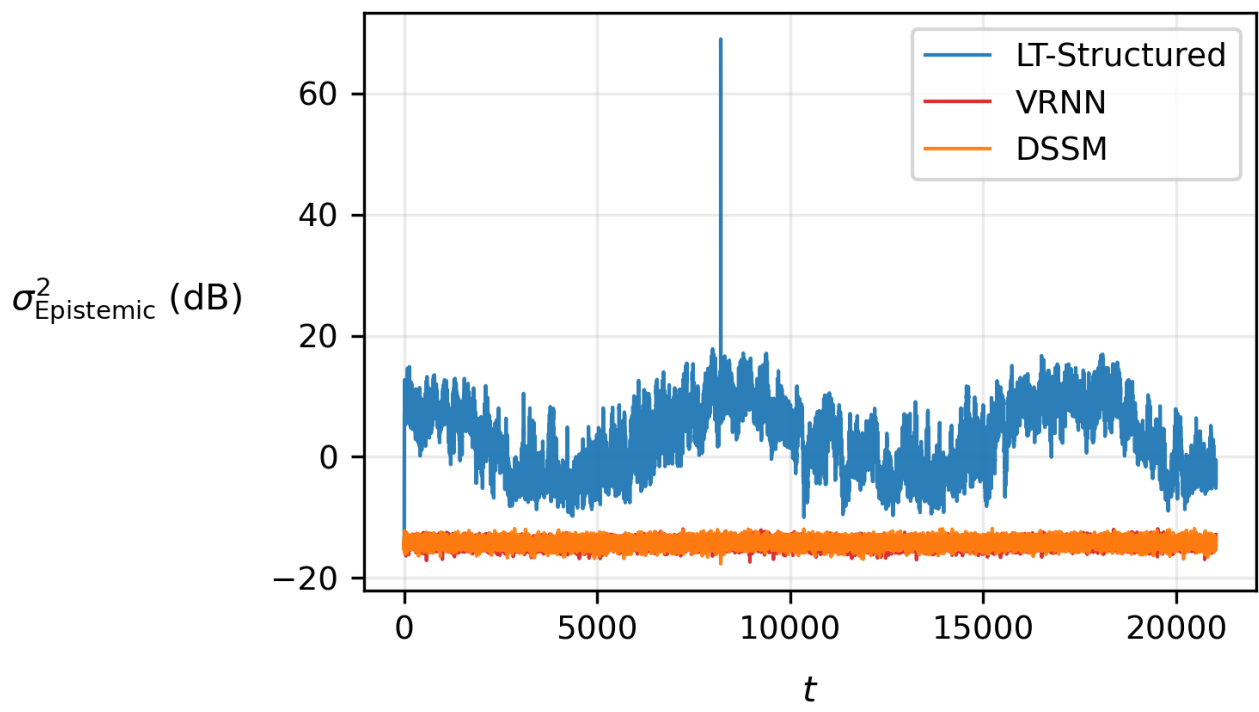

 (a) $\sigma_{\text{Aleatoric}}$ vs t

 (b) $\sigma_{\text{Epistemic}}$ vs t

Figure 6. Decomposition of predictive uncertainty for the representative seed, reported in decibels (dB). (a) Aleatoric variance $\sigma_{\text{Aleatoric}}^2$ over time (dB), reflecting observation noise captured by each model. (b) Epistemic variance $\sigma_{\text{Epistemic}}^2$ over time (dB), reflecting model uncertainty estimated via predictive sampling. LT-Structured exhibits temporally varying epistemic uncertainty with a single isolated spike corresponding to a rare divergence event, while VRNN and DSSM exhibit comparatively low and nearly constant epistemic variance.

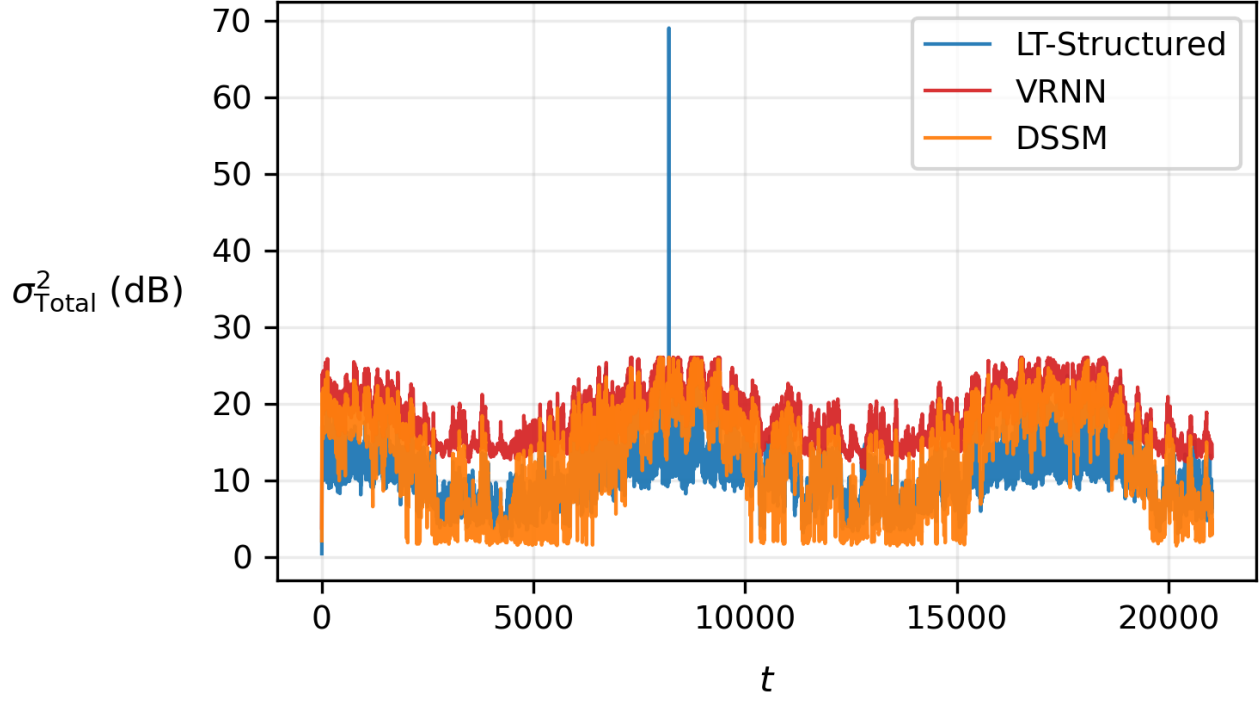
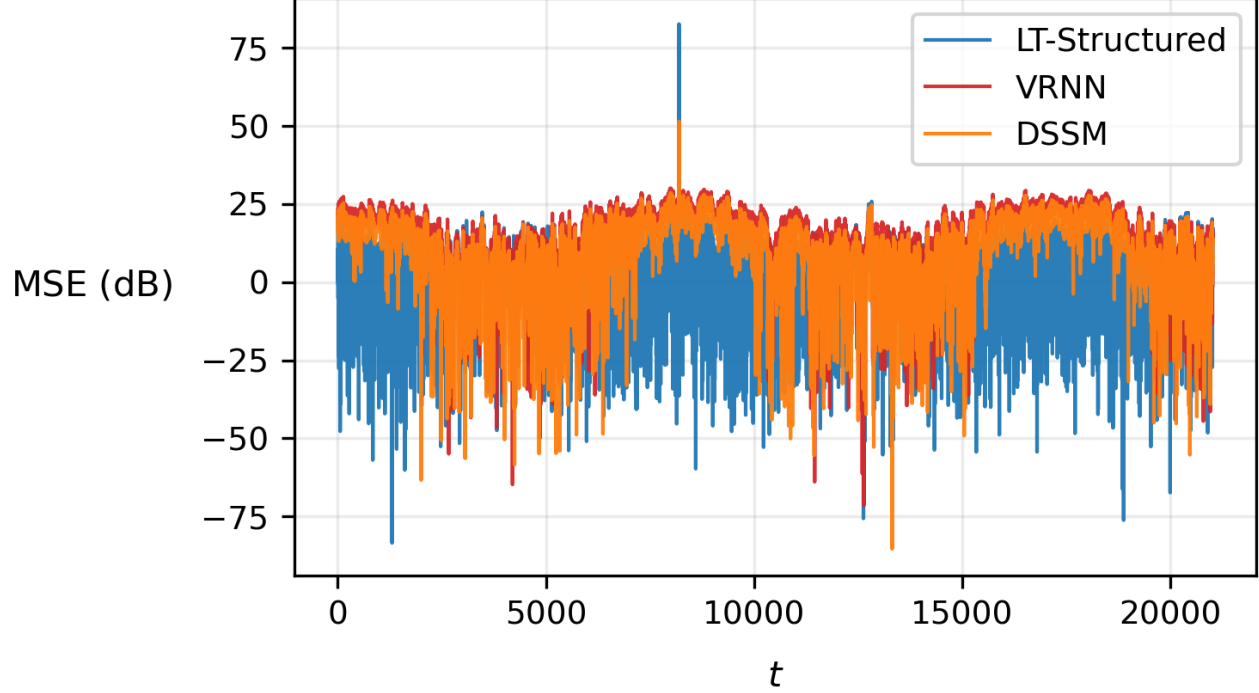

 (a) σ_{Total} vs t

 (b) MSE vs t

Figure 7. Total predictive variance and squared error over time for the representative seed, reported in decibels (dB). (a) Total predictive variance $\sigma_{Total}^2 = \sigma_{Aleatoric}^2 + \sigma_{Epistemic}^2$ as a function of time (dB). (b) Corresponding mean squared error (MSE) over time (dB). LT-Structured exhibits a single isolated spike in both variance and error corresponding to a rare divergence event, while otherwise maintaining stable uncertainty estimates and low error throughout the sequence. VRNN and DSSM exhibit smoother but consistently higher error profiles over time.

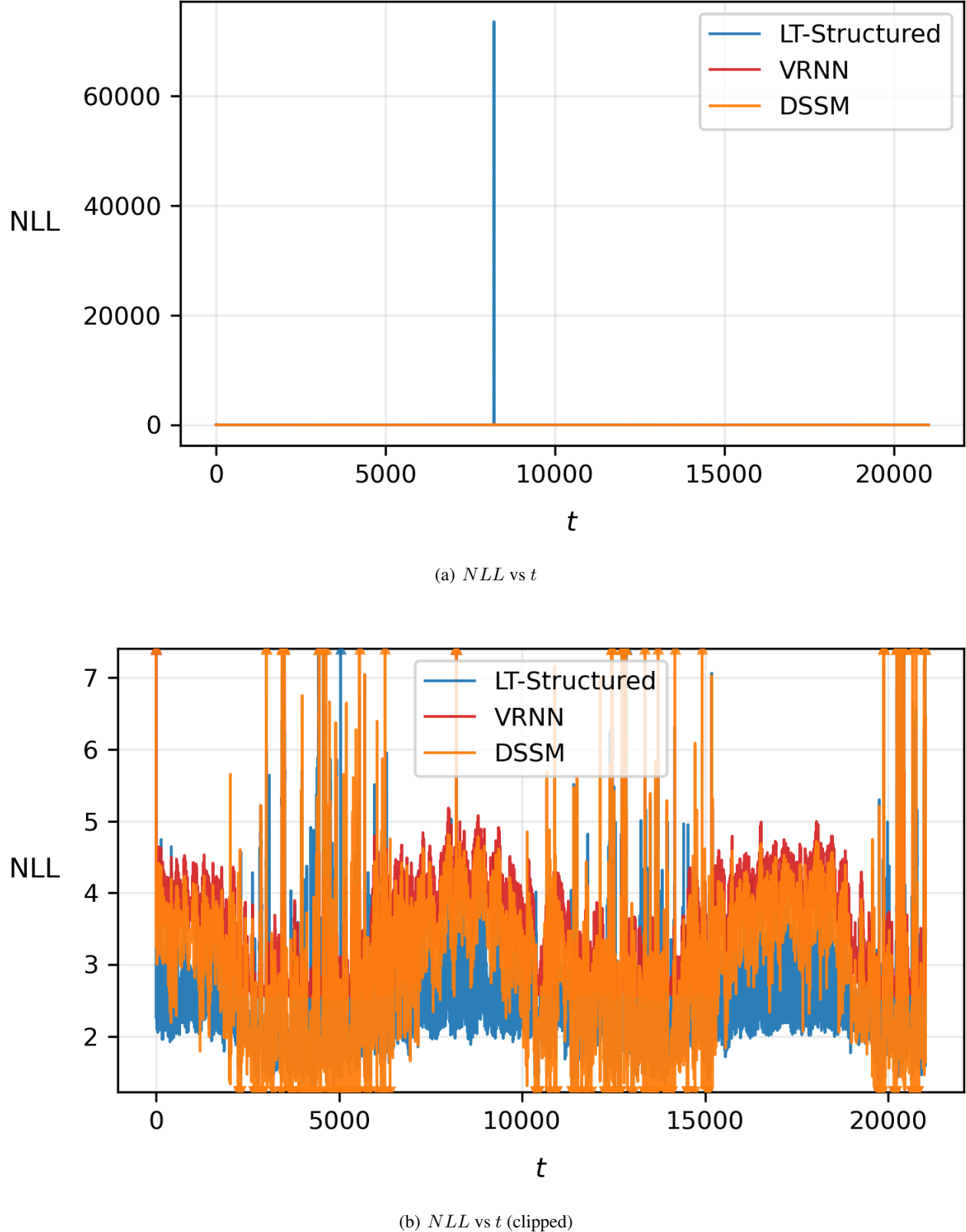
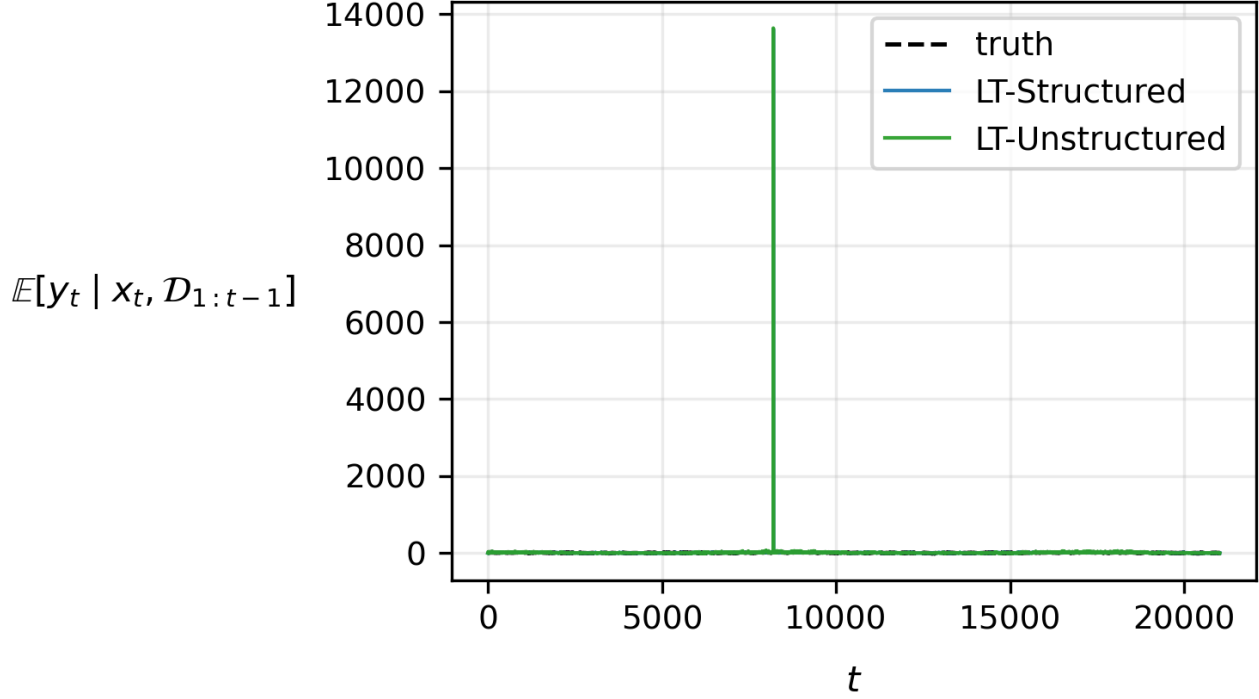
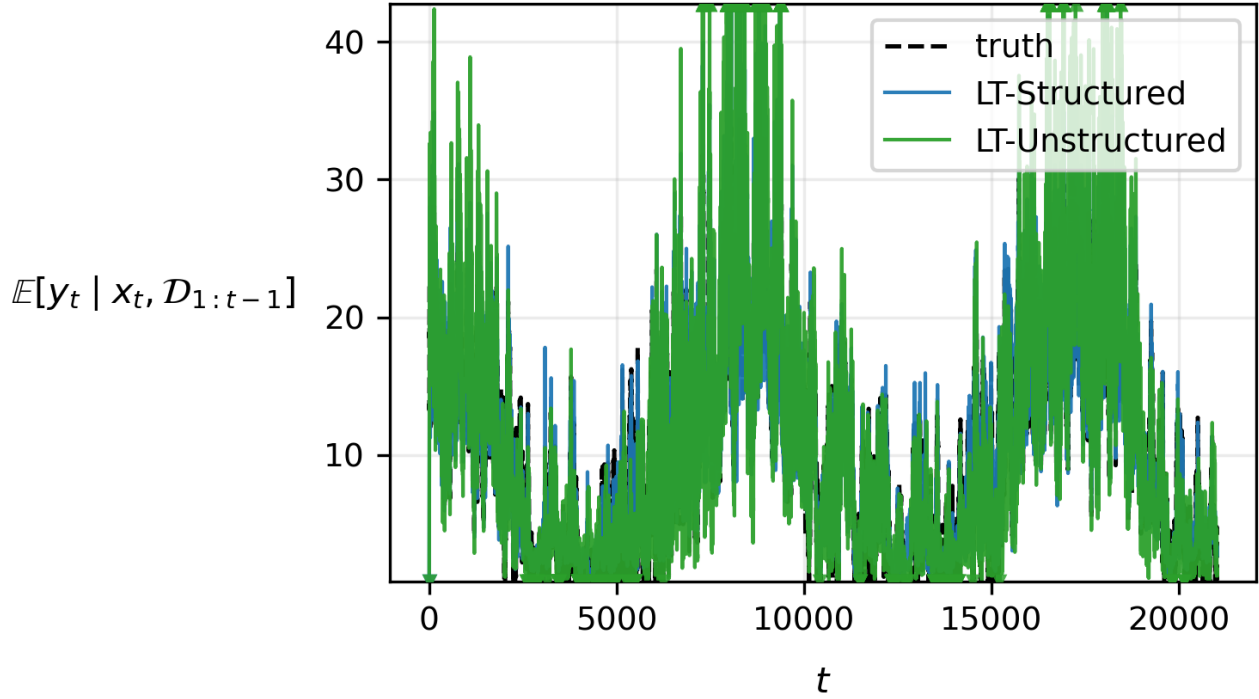


Figure 8. Negative log-likelihood (NLL) trajectories over time for the representative seed. (a) Unclipped NLL as a function of time, illustrating a single isolated divergence event for LT-Structured that produces an extreme NLL spike. (b) Clipped view of the same trajectories to highlight typical per-step likelihood behavior across methods. The isolated spike in (a) dominates untrimmed temporal NLL statistics, while the clipped view in (b) shows that LT-Structured otherwise maintains consistently lower NLL over time relative to VRNN and DSSM.



(a) Predictive mean vs t



(b) Predictive mean vs t (clipped)

Figure 9. Predictive mean trajectories comparing LT variants for the representative seed. (a) Unclipped predictive mean $E[y_t | x_t, \mathcal{D}_{1:t-1}]$ over the full time horizon, illustrating an isolated divergence event for the unstructured variant. (b) Clipped view of the same trajectories to highlight typical predictive behavior. LT-Structured exhibits more stable tracking over time, while LT-Unstructured is more prone to large transient deviations; nevertheless, both variants maintain lower typical error than stateful baseline models under comparable clipping.

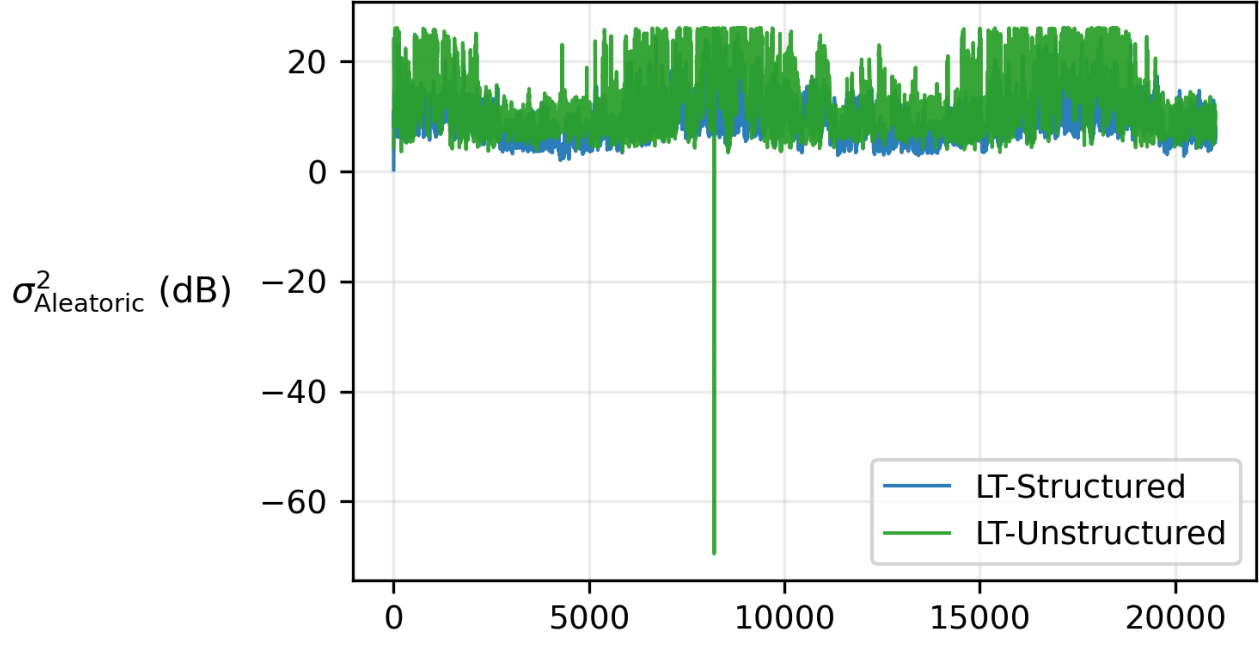
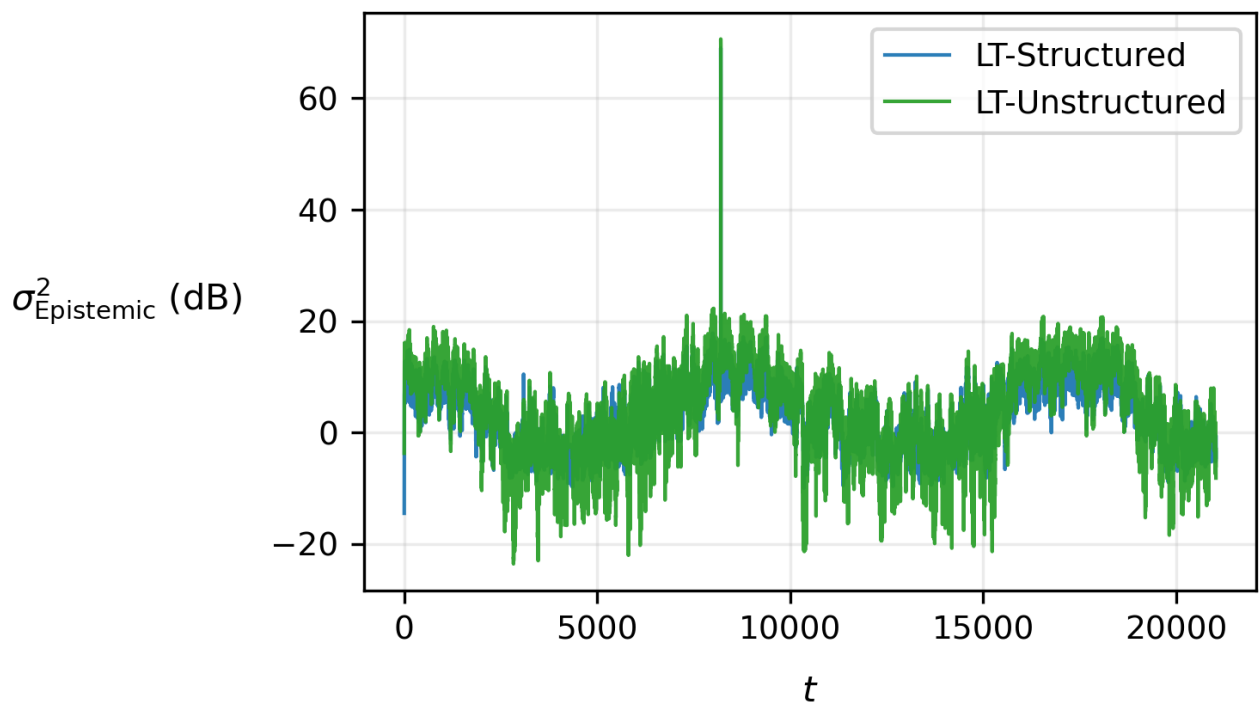

 (a) $\sigma_{\text{Aleatoric}}$ vs t

 (b) $\sigma_{\text{Epistemic}}$ vs t

Figure 10. Decomposition of predictive uncertainty for LT variants on the representative seed, reported in decibels (dB). (a) Aleatoric variance $\sigma_{\text{Aleatoric}}^2$ over time (dB), reflecting observation noise captured by each model. (b) Epistemic variance $\sigma_{\text{Epistemic}}^2$ over time (dB), reflecting model uncertainty estimated via predictive sampling. LT-Structured exhibits smoother and more stable uncertainty estimates over time, while LT-Unstructured shows larger transient fluctuations and an isolated spike corresponding to a rare divergence event.

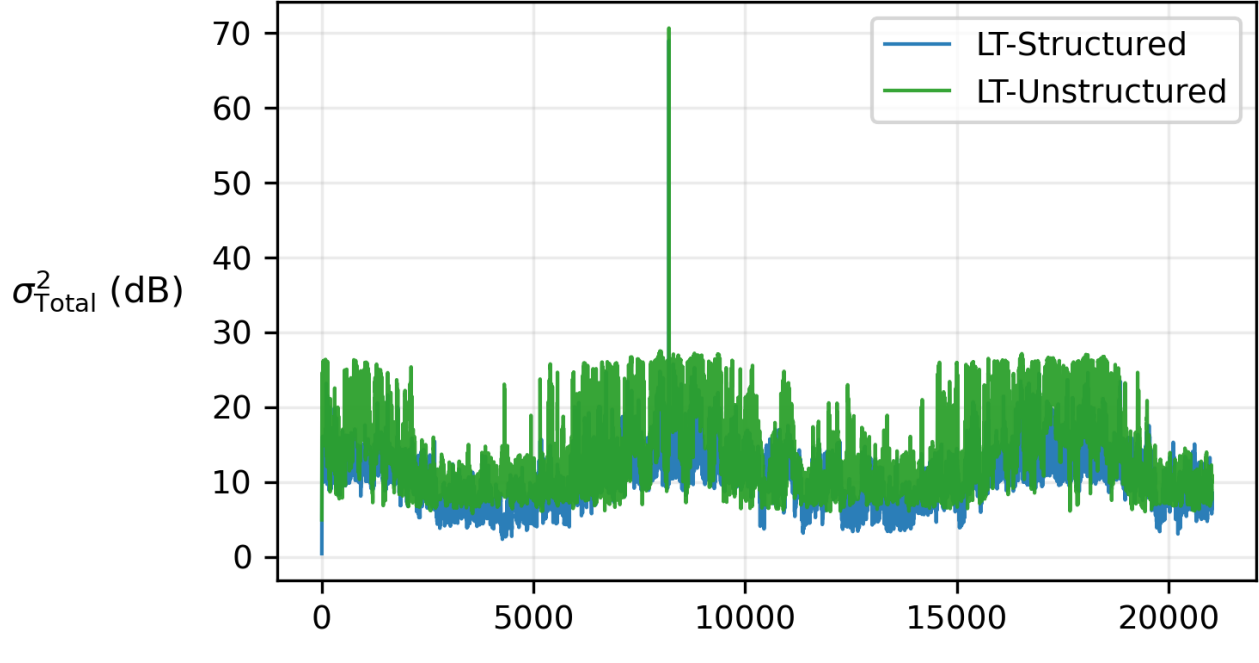
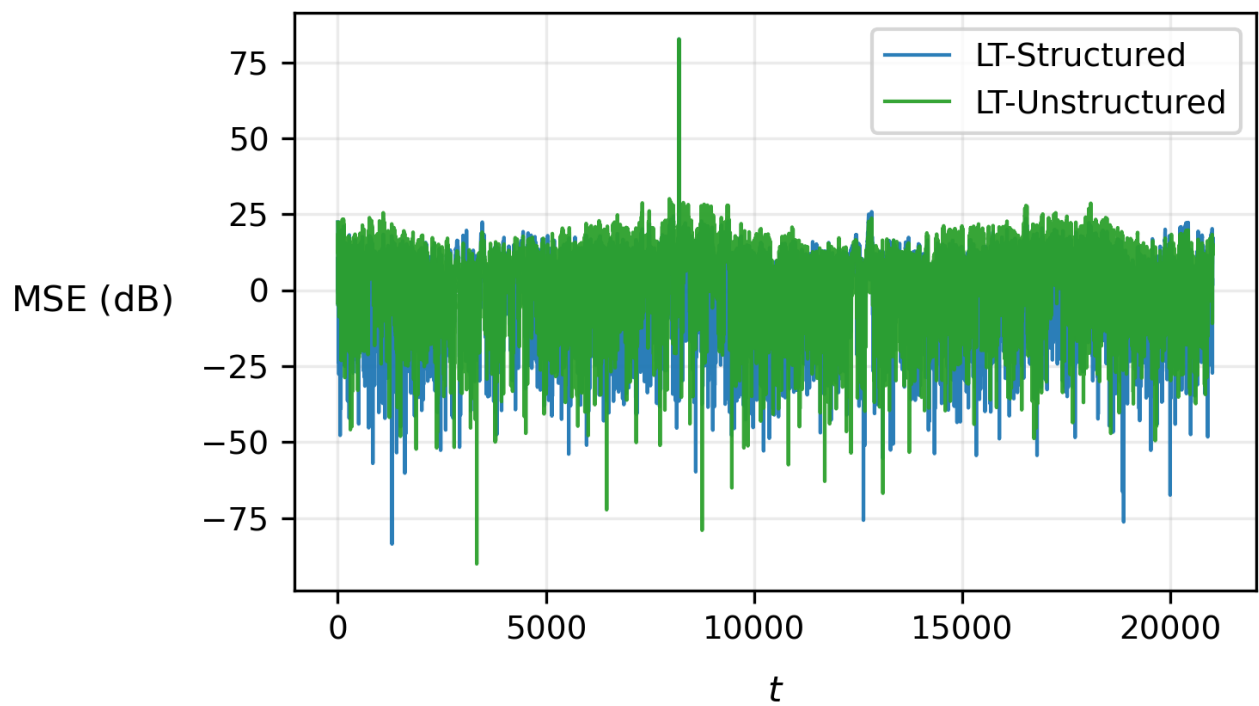

 (a) σ_{Total} vs t

 (b) MSE vs t

Figure 11. Total predictive variance and squared error over time for LT variants on the representative seed, reported in decibels (dB). (a) Total predictive variance $\sigma_{Total}^2 = \sigma_{Aleatoric}^2 + \sigma_{Epistemic}^2$ as a function of time (dB). (b) Corresponding mean squared error (MSE) over time (dB). LT-Unstructured exhibits a larger transient spike in both variance and error corresponding to a rare divergence event, while LT-Structured maintains more stable uncertainty estimates and lower typical error throughout the sequence.

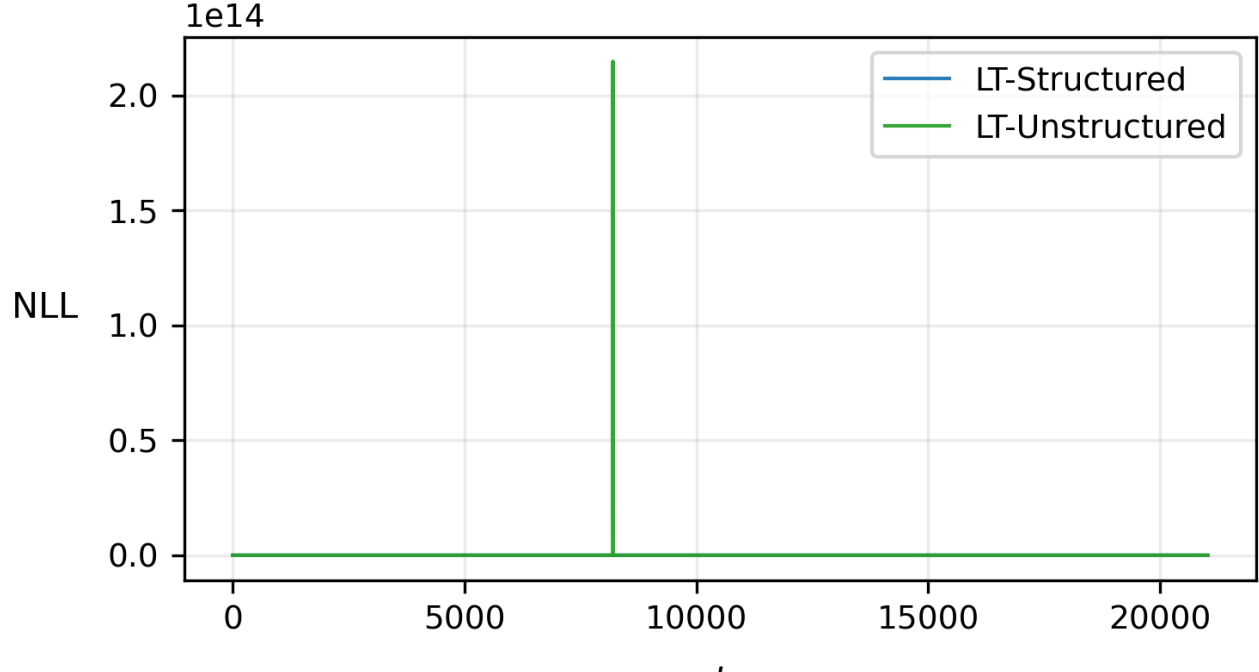
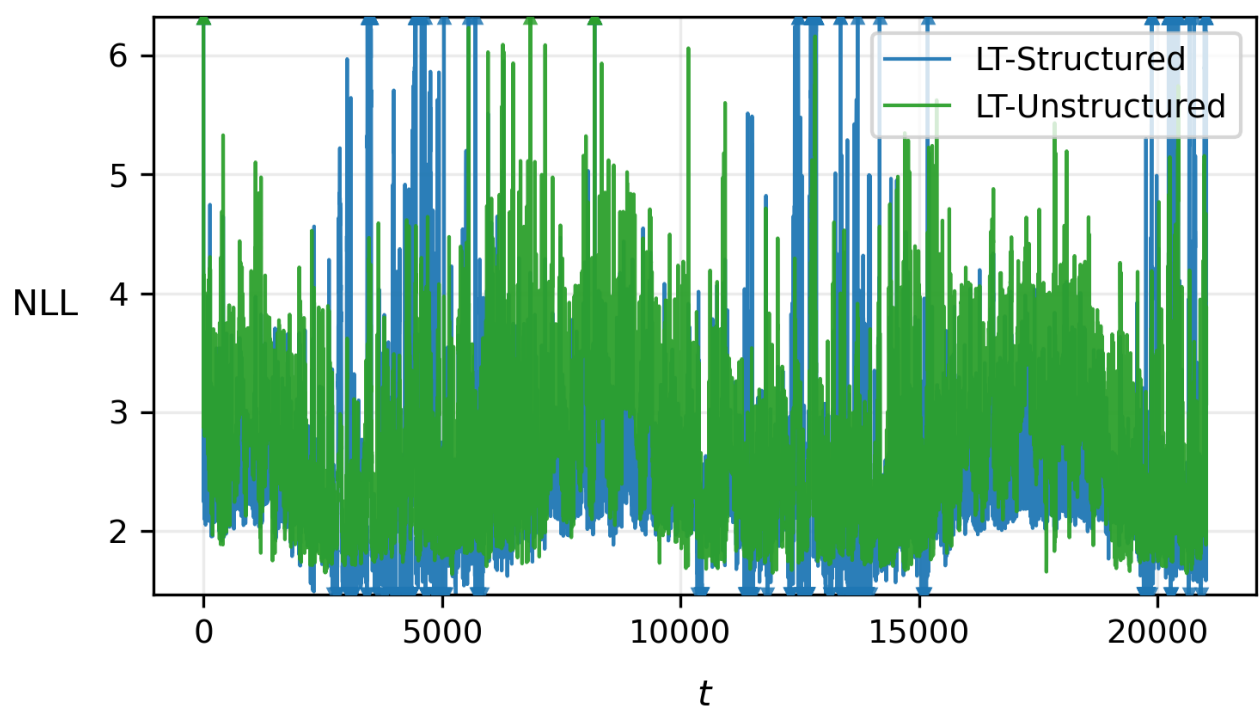

 (a) NLL vs t

 (b) NLL vs t (clipped)

Figure 12. Negative log-likelihood (NLL) trajectories over time comparing LT variants for the representative seed. (a) Unclipped NLL as a function of time, illustrating a single isolated divergence event for the unstructured variant that produces an extreme NLL spike. (b) Clipped view of the same trajectories to highlight typical per-step likelihood behavior. LT-Structured maintains more stable and consistently lower typical NLL over time, while LT-Unstructured is more prone to large transient deviations despite similar average behavior under clipping.

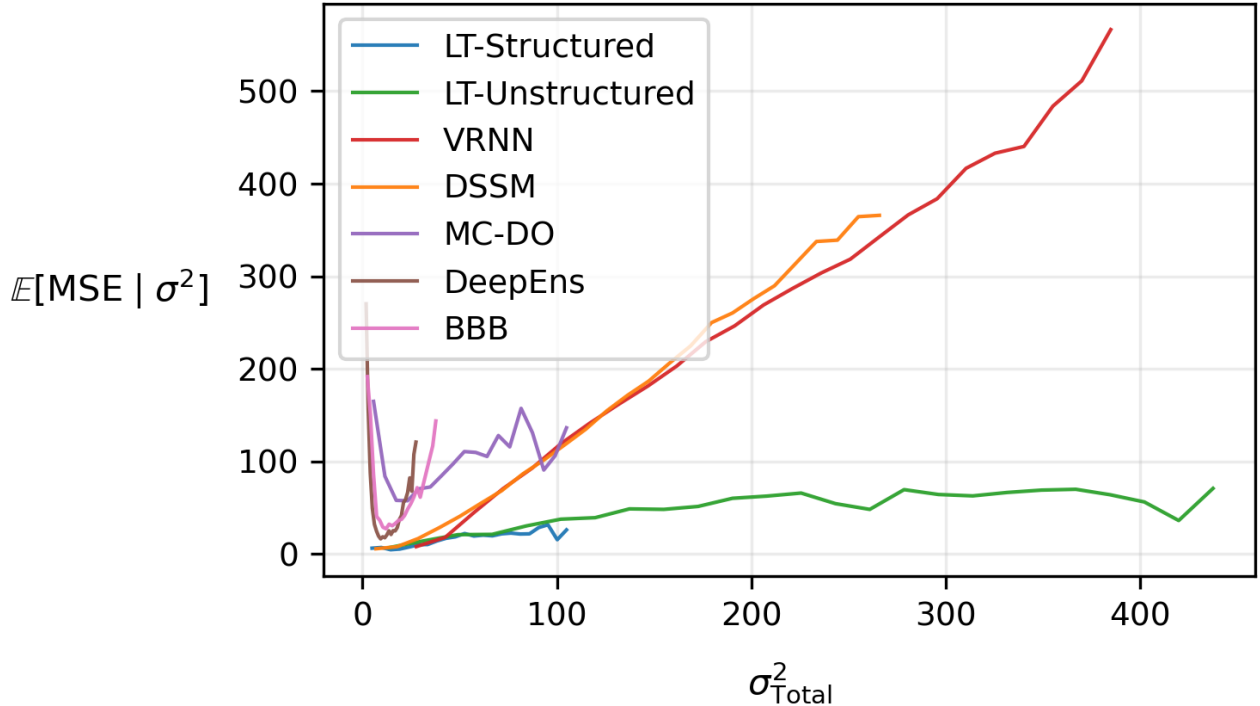


Figure 13. Empirical relationship between predictive uncertainty and squared error for the representative seed. The plot shows $E[\text{MSE} | \sigma_{\text{total}}^2]$ as a function of total predictive variance σ_{total}^2 , both reported in linear scale, estimated by binning time steps according to predicted variance. To emphasize typical behavior, values are clipped to the [1, 99] percentile range prior to binning. Well-calibrated uncertainty corresponds to a monotonic and approximately proportional relationship between predicted variance and observed error. LT-Structured exhibits a comparatively shallow and stable error–variance relationship across uncertainty levels, whereas DSSM and VRNN display substantially steeper growth, indicative of poorly scaled uncertainty under high variance.

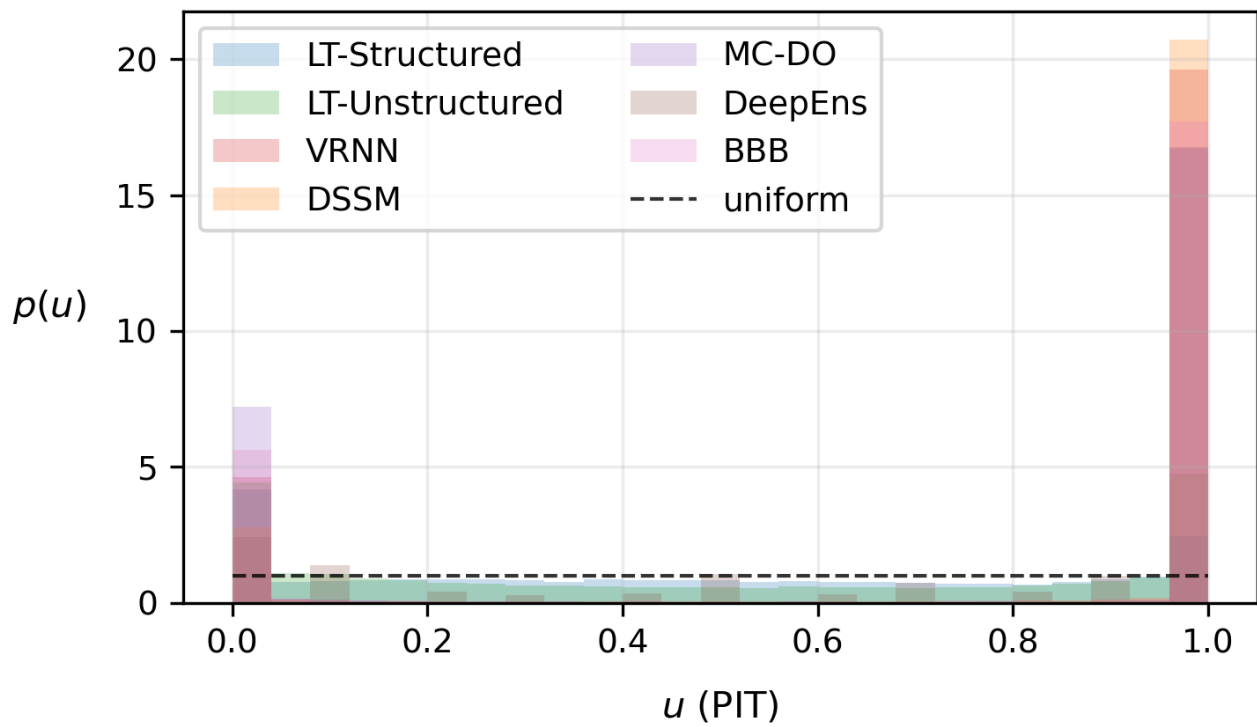


Figure 14. Probability integral transform (PIT) histograms for predictive distributions on the representative seed. For a well-calibrated probabilistic model, PIT values u should be approximately uniformly distributed on $[0, 1]$ (dashed line). LT-Structured produces a comparatively flatter PIT distribution, indicating improved calibration of predictive uncertainty, whereas several baseline methods exhibit pronounced boundary mass consistent with under- or overconfident predictions.

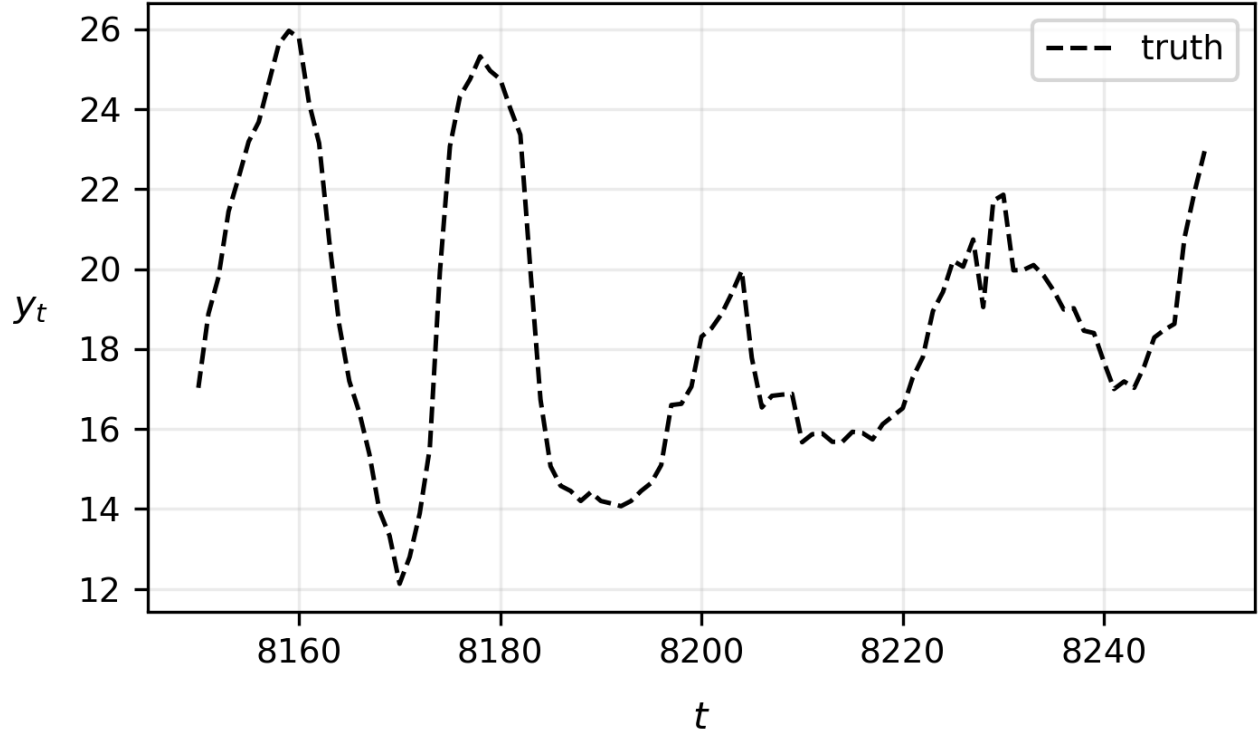
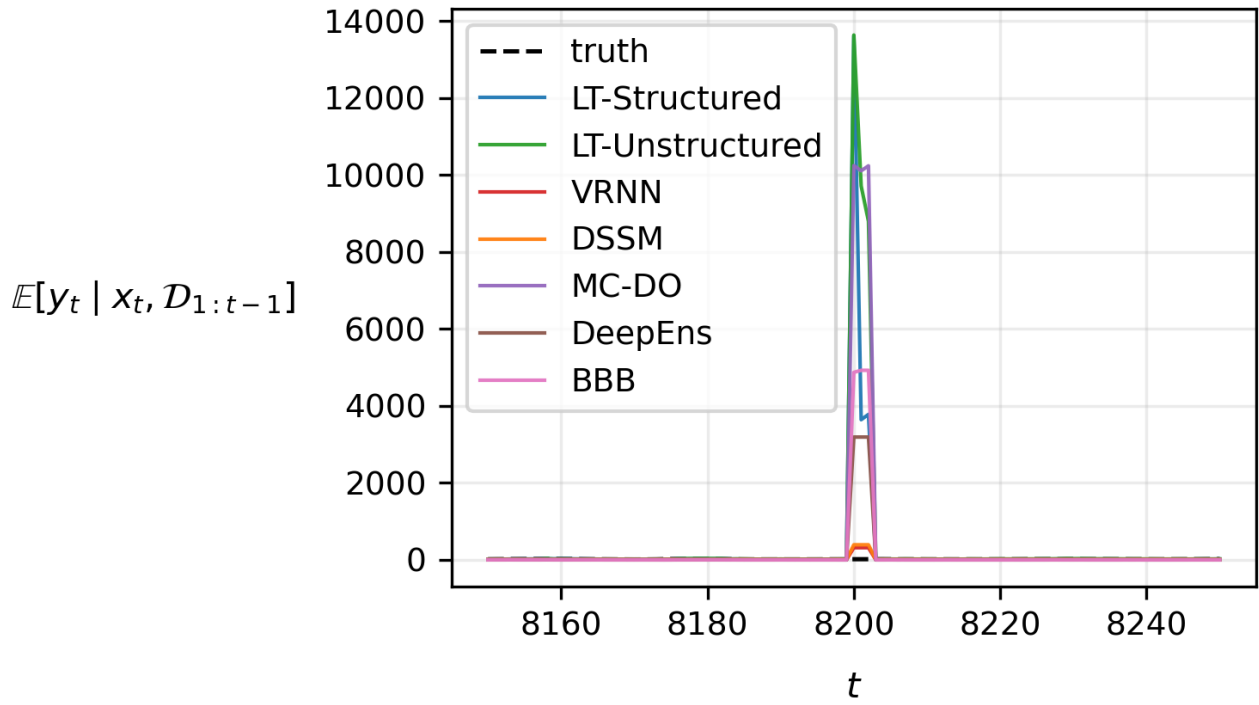

 (a) Truth vs t

 (b) Predictive mean vs t

Figure 15. Ground-truth signal and predictive mean trajectories around an isolated extreme observation. Top: ground-truth target values y_t over the selected time window. Bottom: predictive means $\mathbb{E}[y_t | x_t, \mathcal{D}_{1:t-1}]$ for all models at the same time indices. All models exhibit a sharp transient deviation at the same time step, reflecting a shared response to the extreme observation rather than model-specific instability.

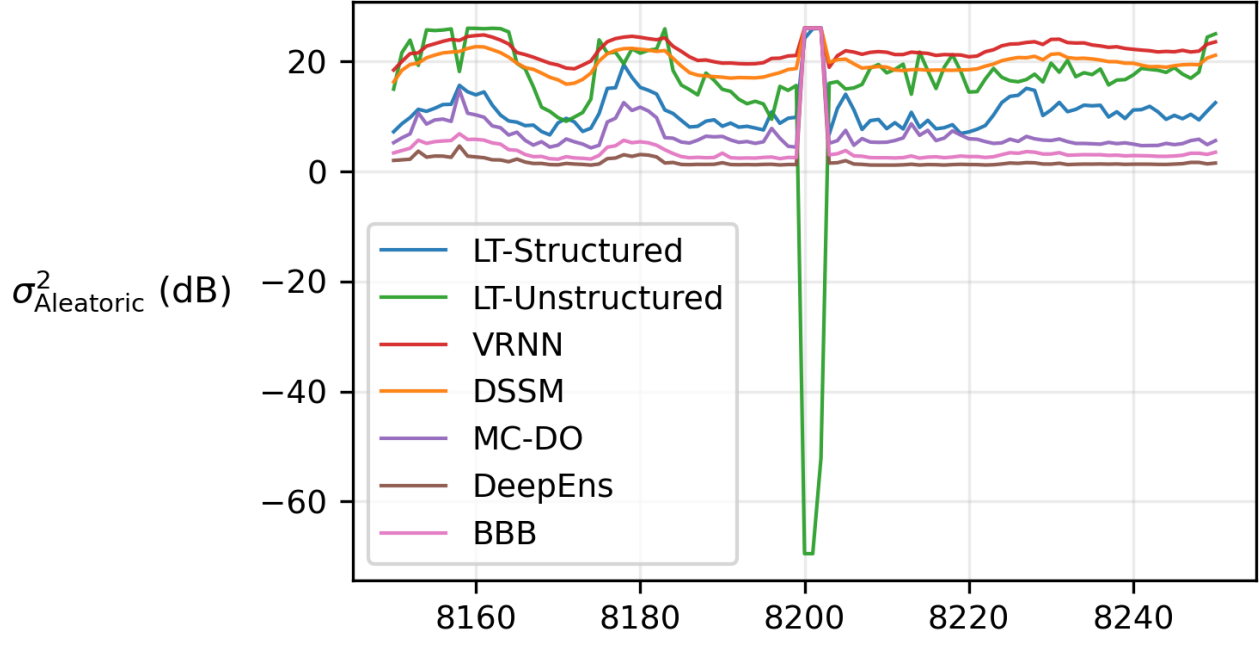
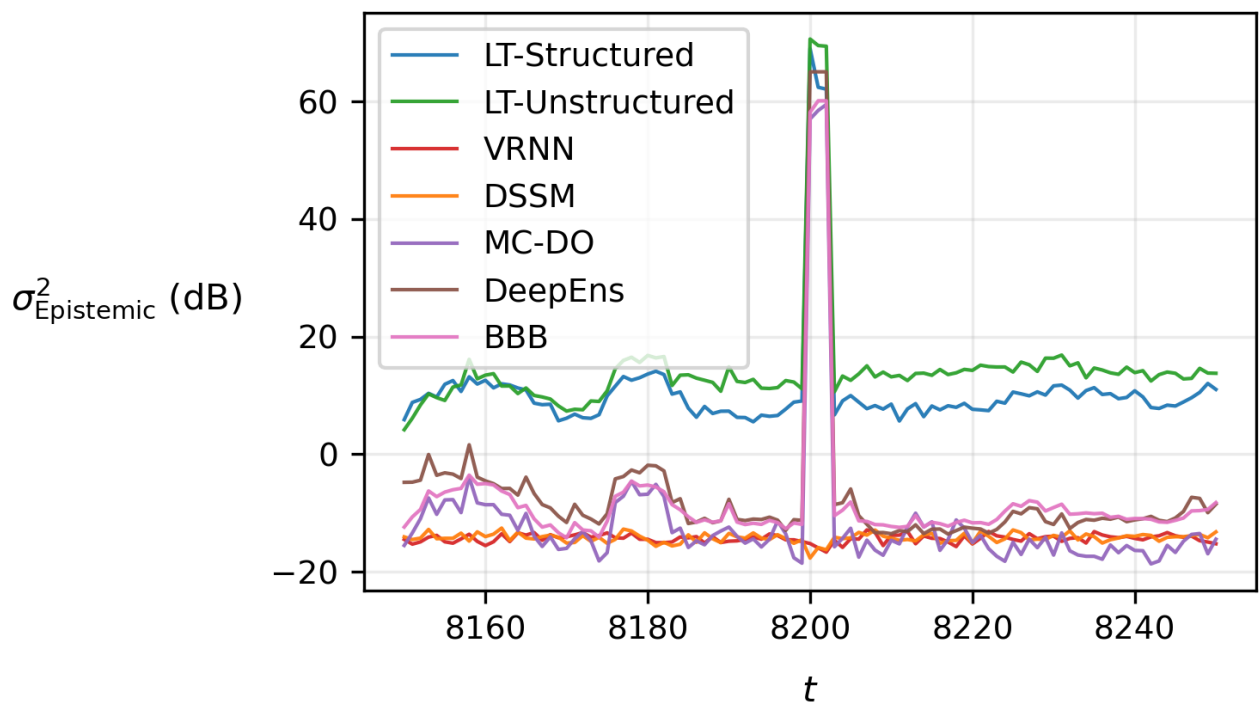

 (a) $\sigma_{Aleatoric}$ vs t

 (b) $\sigma_{Epistemic}$ vs t

Figure 16. Decomposition of predictive uncertainty around an isolated extreme observation (all quantities shown in dB). Top: aleatoric variance $\sigma_{Aleatoric}^2$ over time (dB). Bottom: epistemic variance $\sigma_{Epistemic}^2$ over time (dB). All models—including both stateful and static baselines—exhibit anomalous behavior at the same time step, indicating sensitivity to a shared extreme observation rather than model-specific instability. In all cases, uncertainty rapidly returns to baseline levels following the event, consistent with transient stress rather than persistent miscalibration.

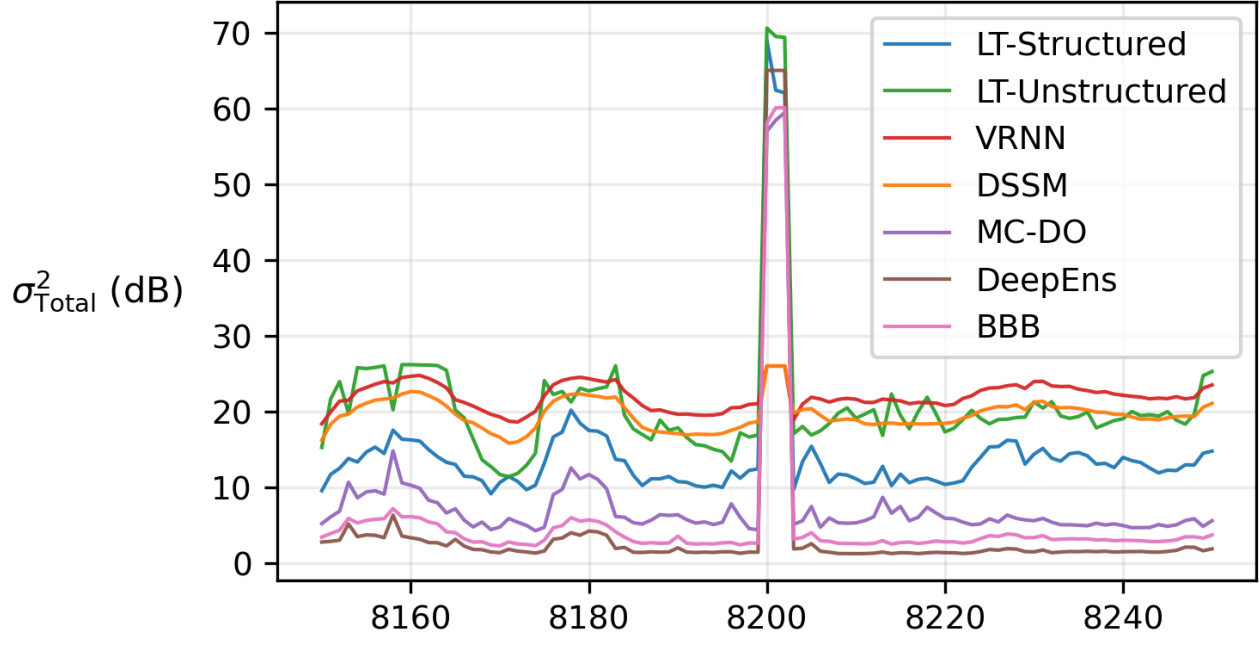
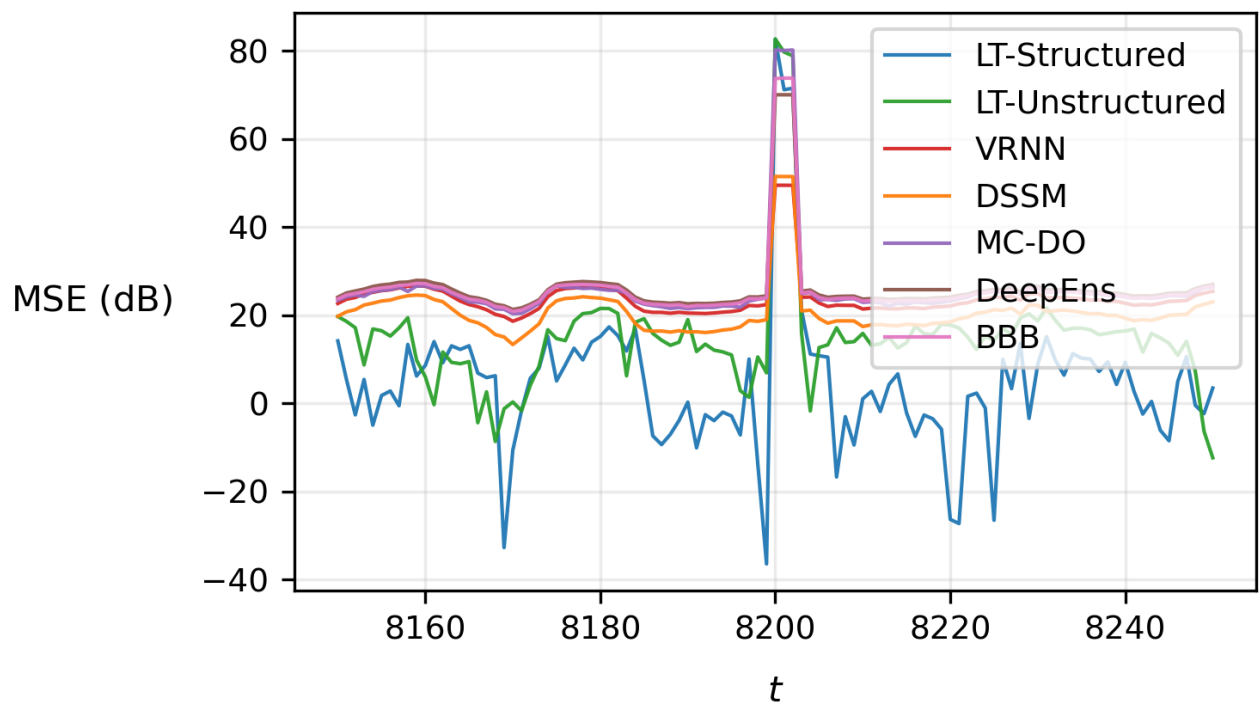

 (a) σ_{Total} vs t

 (b) MSE vs t

Figure 17. Temporal evolution of total predictive uncertainty and error around an isolated extreme observation (all quantities shown in dB). Top: total predictive variance σ_{Total}^2 over time (dB). Bottom: mean squared error (MSE) over time (dB). All models exhibit a sharp, synchronized spike at the same time step, indicating sensitivity to a shared extreme observation rather than model-specific instability. Following this event, both predictive uncertainty and error rapidly return to their typical ranges, consistent with a transient anomaly rather than sustained degradation in predictive performance.

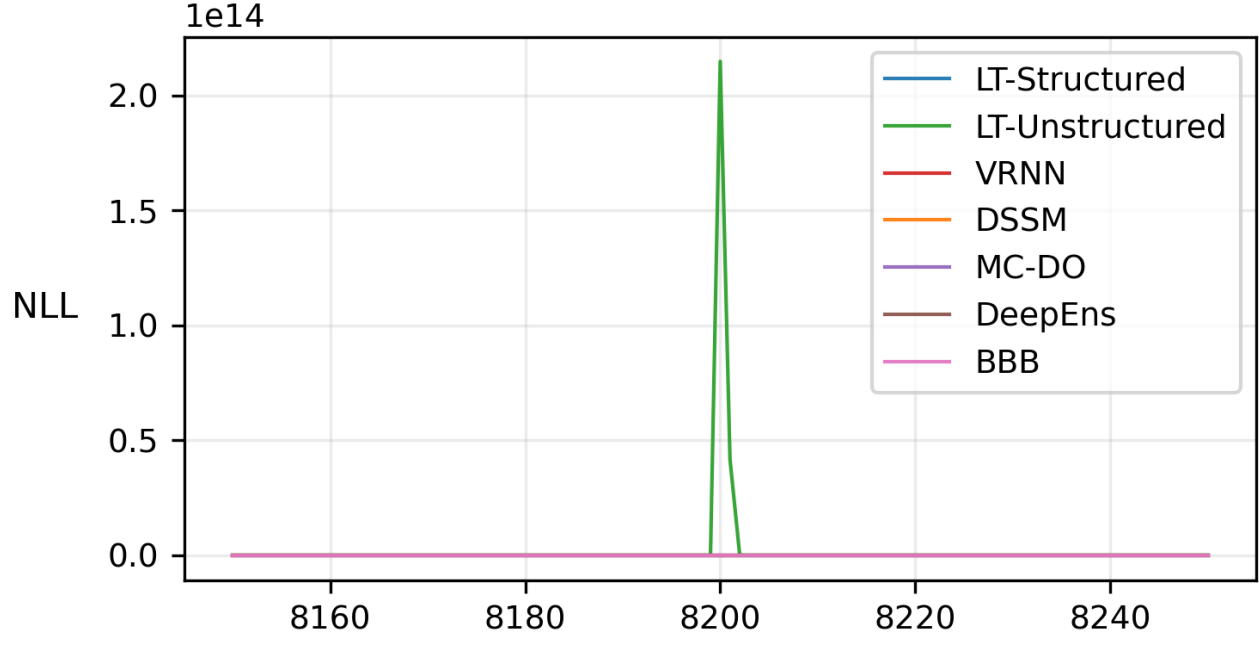
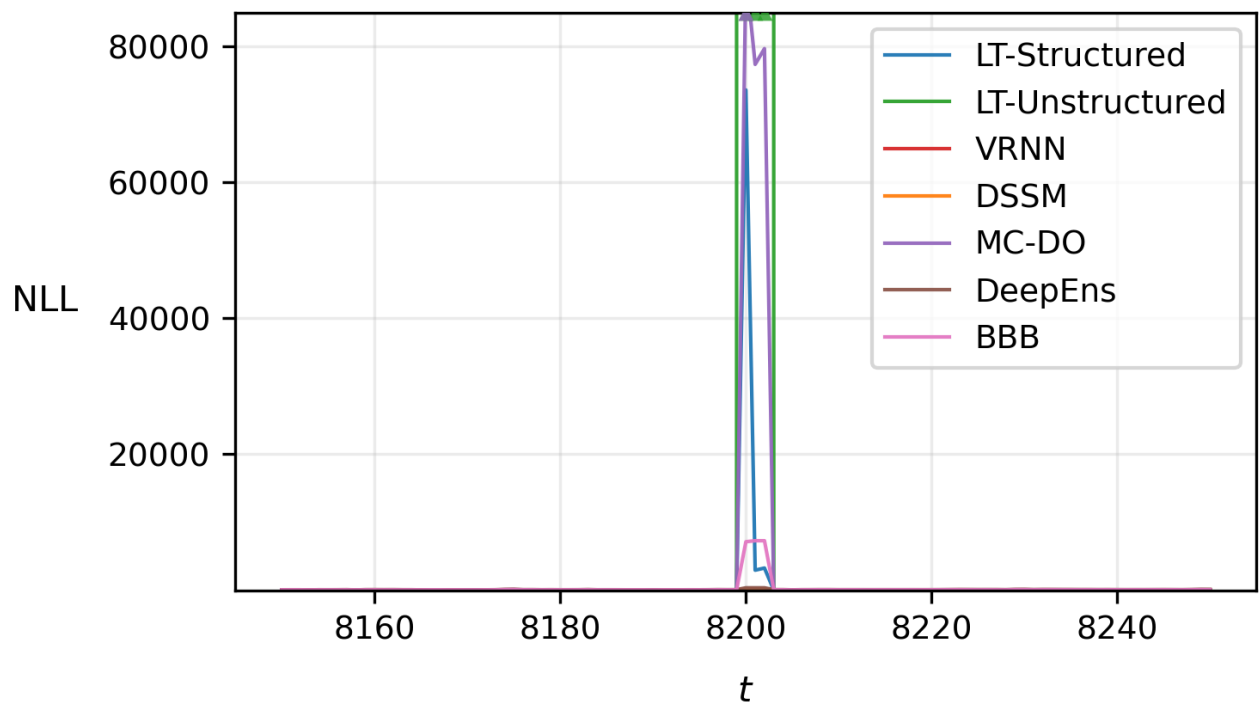
(a) NLL vs t (b) NLL vs t (clipped)

Figure 18. Negative log-likelihood (NLL) around an isolated extreme observation. Top: NLL over time shown on the full scale, highlighting a single catastrophic spike that dominates the dynamic range. Bottom: the same NLL with the vertical axis clipped to reveal relative behavior across models outside the extreme event. All models exhibit a synchronized spike at the same time step, indicating sensitivity to a shared anomalous observation rather than model-specific instability. Outside this isolated event, NLL values remain well-behaved and return rapidly to baseline levels.